

APPLICATION OF POLARIMETRY TO SURVEILLANCE
AND UNDERWATER IMAGING

by

Yitian Ding

Copyright © Yitian Ding 2019

A Dissertation Submitted to the Faculty of the

JAMES C. WYANT COLLEGE OF OPTICAL SCIENCES

In Partial Fulfillment of the Requirements

For the Degree of

DOCTOR OF PHILOSOPHY


In the Graduate College

THE UNIVERSITY OF ARIZONA


2019

THE UNIVERSITY OF ARIZONA
GRADUATE COLLEGE

As members of the Dissertation Committee, we certify that we have read the dissertation prepared by *Yitian Ding* titled *Application of Polarimetry to Surveillance and Underwater Imaging* and recommend that it be accepted as fulfilling the dissertation requirement for the Degree of Doctor of Philosophy.



Stanley Pau Date: 07/23/19




Amit Ashok Date: 07/23/2019



Russell Chipman Date: 07/23/2019

Final approval and acceptance of this dissertation is contingent upon the candidate's submission of the final copies of the dissertation to the Graduate College.

I hereby certify that I have read this dissertation prepared under my direction and recommend that it be accepted as fulfilling the dissertation requirement.



Stanley Pau Date: 07/23/19
Dissertation Committee Chair
Optical Sciences/Electrical and Computer Engineering

ARIZONA

ACKNOWLEDGEMENTS

I would like to thank my advisor, Prof. Stanley Pau, for his patience, advice and support through this research. He's always been looking at the essence of the problems, and without his guidance this dissertation would be impossible. All lab members, Xingzhou Tu, Dr. Linan Jiang and Sawyer Miller, have also been a great help and I genuinely appreciate it.

I would like to thank Prof. Amit Ashok for his help during our collaboration on the DARPA project, Prof. Russell A. Chipman and Dr. Greg A. Smith for the enlightening course series on polarization optics, and Prof. R. John Koshel for his help on the study of optical scattering and stray light.

Additional thanks go to Mohan Xu, Ronan Kerviche, Hekun Huang, Xiaobo Tian, Dr. Bofan Song, Jingwei Wu, Shu Yang, Hwang-Jye Yang, Yukun Qin, Qi Cui, and other colleagues in the College for their support.

Finally, my special gratitude goes to Miaomiao Xu, for the company through the years that accounts for many of the "It's worth it!" moments.

DEDICATION

To my parents,

丁健 and 钱青,

Who have always had faith in me

Table of Contents

List of Figures.....	7
List of Tables	9
Abstract.....	10
Chapter 1. Introduction	12
1.1 The electromagnetic wave.....	12
1.2 Polarization states of monochromatic light	14
1.3 Fresnel equations.....	17
1.4 Stokes vectors and Mueller matrices	20
1.5 Transmission and reflection Mueller matrices.....	24
Chapter 2. Polarization-based image separation with unpolarized objects	25
2.1 Background	25
2.2 Mueller matrix equations for image separation with unpolarized objects	28
2.3 Evaluation of image correlation.....	33
2.4 Separation algorithm.....	35
2.5 Collection of separation results	36
2.6 The SNR limit of separation.....	44
2.7 Image separation in the scenes with multiple reflectors	46
2.8 Discussion and Conclusions.....	48
Chapter 3. Polarization-based image separation with polarized objects.....	50
3.1 Polarized sources.....	50
3.2 Mueller matrices	54
3.3 Mueller matrix equations for image separation with polarized objects.....	56
3.4 Collection of separated images	59
3.5 Application of filtering	63
Chapter 4. Total internal reflection in Nature	67
4.1 Background	67
4.2 Total internal reflection in inferior mirages.....	69

4.3 Other examples of TIR in Nature	72
Chapter 5. Circular polarization under water	74
5.1 Distribution of circular polarization under water	74
5.2 The Umov effect	78
5.3 Collection of Stokes images	81
Chapter 6. Study of air bubbles under water	87
6.1 Distribution of DoCP around a bubble.....	87
6.2 Average DoCP across a bubble	88
Chapter 7. Closing remarks	90
References	91

List of Figures

Fig. 1.1. Local coordinate systems on an interface.	18
Fig. 2.1. Schematic of the scene.	29
Fig. 2.2. Separation algorithm.	36
Fig. 2.3. Separation of indoor scenes.	38
Fig. 2.4. Patch-wise separation of trees from a window.	40
Fig. 2.5. A hallway scene consisting of fluorescent lights, an exit sign on the ceiling, and glossy floor.	41
Fig. 2.6. Comparison of the separation results for different incident angles.	42
Fig. 2.7. Separation with diffuse surfaces.	43
Fig. 2.8. SNR for reflectors that have both specular and diffuse components in LWIR.	45
Fig. 2.9. Number of unknowns and number of equations as functions of the number of reflectors.	47
Fig. 3.1. A schematic of the scene is shown.	51
Fig. 3.2. Reflection of the monitor screen from a marble tile is shown.	60
Fig. 3.3. Reflection of the laptop screen (displaying ISO 12233 test chart) from a glass-covered picture is shown.	61
Fig. 3.4. Reflection of a cell phone screen (displaying a login screen with the username and the password) from a wood sample (overlapping region shown in red rectangle) is shown.	62
Fig. 3.5. Results with Wiener filtering.	65
Fig. 4.1. Schematic of the multiple-layered dielectric plate model.	70
Fig. 4.2. Retardance under various N.	72
Fig. 5.1. Schematic of the scene.	75
Fig. 5.2. $ \sin \delta(\theta_i) $ and $f(\phi)$	77
Fig. 5.3. Variation of the maximum DoCP versus ϕ (orange) and the maximum DoCP location versus ϕ (blue).	77
Fig. 5.4. DoLP and DoCP as functions of α and ψ	78
Fig. 5.5. Experimental configurations and corresponding camera views.	81
Fig. 5.6. Stokes images of a ceramic cylinder and two ceramic spheres under water.	82
Fig. 5.7. Stokes images of four black mussels under water.	83

Fig. 5.8. Stokes images of four white clams underwater.	84
Fig. 5.9. Stokes images of two stones and two black mussels under water.	85
Fig. 5.10. Inverse relationship between DoCP and albedo of four samples underwater.	86
Fig. 6.1. Schematic of the refraction/reflection and TIR on an underwater air bubble under collimated laser illumination.	87
Fig. 6.2. Conversion efficiency as a function of incident angle.	88

List of Tables

Table 3.1. MAD of the indoor and outdoor scenes using the EO methods	43
--	----

Abstract

This dissertation discusses two major topics: The separation of images with polarimetric imaging and the total internal reflection under water. It is organized as follows. Chapter 1 is the introduction and it talks about the basics of polarization optics. It starts with the Maxwell's equations to derive the wave equation of plane electromagnetic waves, and then talks about the Jones vectors and Jones matrices, which describe the polarization properties of monochromatic waves and of optical components that are illuminated by the waves. The Fresnel reflection is then discussed using the Jones calculus. After that, the discussion is extended to polychromatic light, where the Stokes vectors and Mueller matrices are used instead. The Mueller matrices for Fresnel reflection is given at last.

In chapter 2 and chapter 3, image separation with unpolarized objects and polarized objects are studied. The Mueller matrix equations for scenes with various reflectors are derived, and the algorithms that solve the corresponding scalar equations for separated images are developed. In the algorithms, the correlation between images is evaluated by a metric function – edge overlap – that is developed specifically for this image separation application. A variety of test scenes and separation results are shown to demonstrate the advantages and disadvantages of the proposed separation method. In addition, a limit of this method imposed by the signal-to-noise ratio of the captured images is estimated. At the end, the extension of the proposed method to scenes with multiple reflectors are discussed.

Chapter 4 serves as the introduction to the second topic. It goes over the situations in Nature that total internal reflection could happen, and briefly studies the related polarization effects.

Chapter 5 and chapter 6 then focus on the total internal reflection at the water-air interface. In chapter 5, the conversion from linearly polarized light to circularly/elliptically polarized light in total internal reflection is studied, and a maximum conversion efficiency is calculated. A maximum degree-of-circular-polarization circle is predicted in the captured reflected image, and the relation between the degree-of-circular-polarization of the reflected light and the surface properties of the captured objects in the image are found to resemble the Umov effect. Meanwhile, chapter 6 calculates the same conversion efficiency across a water bubble and computes various “average” conversion efficiencies. Finally, chapter 7 summarizes the above studies.

The study of image separation has found applications in surveillance while the study of total internal reflection is currently mainly of academic interests. However, the additional information in the polarization properties of light has not been fully appreciated and made use of in most optical systems. We hope that the studies in this dissertation could shine a light on the future applications of polarization optics.

Chapter 1. Introduction

1.1 The electromagnetic wave

Light can be treated as electromagnetic (EM) waves, which are waves in the EM field. Waves typically refer to the types of motion that transfer energy and are continuous in space and time. One fundamental parameter of a wave is its speed. In vacuum, the speed of EM wave, c , is about 3×10^8 m/s.

EM field is the field that carries the EM interaction and is typically described by a 3-dimensional (3D) complex vector as a function of space and time. Maxwell's equations govern the motion of EM field and thus also the EM waves. For EM waves propagating in the materials that have no free electric charge and free electric current, have linear response, and are homogeneous and non-dispersive, the wave equations for electric field and magnetic field at position \mathbf{r} and time t can be derived from the Maxwell's equations,

$$\nabla^2 \mathbf{E}(\mathbf{r}, t) - \epsilon\mu \frac{\partial^2 \mathbf{E}(\mathbf{r}, t)}{\partial t^2} = 0, \quad (1.1.1)$$

$$\nabla^2 \mathbf{H}(\mathbf{r}, t) - \epsilon\mu \frac{\partial^2 \mathbf{H}(\mathbf{r}, t)}{\partial t^2} = 0, \quad (1.1.2)$$

where $\mathbf{E}(\mathbf{r}, t), \mathbf{H}(\mathbf{r}, t)$ are the electric field and magnetic field, $\nabla^2 = \partial^2/\partial x^2 + \partial^2/\partial y^2 + \partial^2/\partial z^2$, and ϵ, μ are the permittivity and permeability of the material. The permittivity and permeability are the metrics of conductivity of electric and magnetic fields in a material. In this dissertation, we focus on the electric field and assume that the materials are non-magnetic, $\mu =$

$\mu_0 \approx 12.57 \times 10^{-7} H/m$, where μ_0 is the permeability in vacuum. It is worth noting that $\epsilon_0 \approx 8.85 \times 10^{-12} F/m$ is the permittivity in vacuum and $c = 1/\sqrt{\epsilon_0\mu_0}$.

The electric field solutions exist in various form. The solutions are typically written as complex-valued functions and the electric field is the real part. The plane wave is a fundamental type of EM waves that propagates in a single direction with a constant amplitude,

$$\mathbf{E}(\mathbf{r}, t) = \mathbf{A} \cdot \exp(i\mathbf{k} \cdot \mathbf{r} - i\omega t), \quad (1.1.3)$$

where \mathbf{A} is the complex amplitude vector, \mathbf{k} is the wave vector, ω is the angular frequency of the wave, and \mathbf{r} and t are the spatial and temporal coordinates. The angular frequency describes the oscillation aspect of waves (the view of waves when \mathbf{r} is fixed), which is related to the energy carried by the wave and is unaffected by the material properties; meanwhile, the propagation aspect of waves (the view of waves when t is frozen) are stored in $k = |\mathbf{k}|$, which is related to the linear momentum of light. The amplitude of the wave vector varies in different materials, $k = n \cdot k_0$, where $n = \sqrt{\epsilon/\epsilon_0}$ is the refractive index of the material. The wave equation of electric field for plane waves thus becomes

$$k = \frac{n}{c} \omega, \quad (1.1.4)$$

as all variants are assumed positive. This relation is sometimes referred to as the dispersion relation. The wavelength of waves is defined as $2\pi/k$ and the period of waves is defined as $2\pi/\omega$.

General EM waves can be decomposed into a collection of plane waves of different angular frequencies as

$$\mathbf{E}(\mathbf{r}, t) = \int \mathbf{A}(\mathbf{r}, t, \omega) \cdot e^{i\mathbf{k}\cdot\mathbf{r} - i\omega t} \cdot d\omega, \quad (1.1.5)$$

or of different wavelengths. It is thus sometimes convenient to consider the monochromatic case (which involves a single wavelength) of an EM wave problem and then extend the results and findings to the polychromatic case.

1.2 Polarization states of monochromatic light

EM waves are transverse waves, which means the electric field has no component along the direction of the wave vector. The electric field is thus limited to the plane that is perpendicular to the wave vector (the transverse plane) and is a 2D vector in that plane. A coordinate system can be defined for the electric field and wave vector as (x, y, z) or (s, p, k) , where x (or s) and y (or p) are the coordinates in the transverse plane and z (or k) is along the wave vector. As \mathbf{k} generally depends on \mathbf{r} , this coordinate system is local. In this dissertation, we use (x, y, z) for an arbitrary local coordinate system and (s, p, k) for the local coordinates on a material interface when studying refraction and reflection. In the transverse plane at a specific \mathbf{r} , the electric field evolves as a function of time, and the vectorial property of the electric field that is independent of the time evolution is the polarization state.

For monochromatic plane waves, the electric field in the local coordinate system at a certain spatial location is

$$\mathbf{E}(t) = \begin{bmatrix} A_x e^{-i\phi_x} \\ A_y e^{-i\phi_y} \end{bmatrix} e^{-i\omega t} = \mathbf{E} e^{-i\omega t}, \quad (1.2.1)$$

where $A_{x,y}$ and $\phi_{x,y}$ are the amplitudes and phases along the local x and y coordinates and \mathbf{E} is the Jones vector. Jones vectors are 2×1 complex vectors that describes the polarization state of monochromatic light. Since the x and y components oscillate with the same angular frequency, the real part of $\mathbf{E}(t)$, in general, forms an ellipse on the transverse plane,

$$\left(\frac{E_x(t)}{E_x(0)}\right)^2 + \left(\frac{E_y(t)}{E_y(0)}\right)^2 - 2 \cdot \frac{E_x(t)}{E_x(0)} \cdot \frac{E_y(t)}{E_y(0)} \cdot \cos \Delta\phi = \sin^2 \Delta\phi, \quad (1.2.2)$$

where $E_{x,y}(t)$ are the x and y components of $\mathbf{E}(t)$, $E_{x,y}(0)$ are the x and y components of $\mathbf{E}(t)$ at $t = 0$ and $\Delta\phi = \phi_x - \phi_y$. The local x and y directions are sometimes referred to as the horizontal and vertical directions when no other coordinate systems are involved.

Depending on the exact pattern formed by the real part of $\mathbf{E}(t)$, we refer to the $\Delta\phi = 0$ polarization states as linear polarization states, the $\Delta\phi = \pi/2$ polarization states as the right-hand circular polarization states, the $\Delta\phi = -\pi/2$ polarization states as the left-hand circular polarization states, and other polarization states as the elliptical polarization states. An elliptical polarization state can be seen as having a linear polarization state and a circular polarization state as its components. The Jones vectors for the horizontal linear polarization state and the right-hand/left-hand circular polarization states are

$$\begin{bmatrix} 1 \\ 0 \end{bmatrix}, \frac{1}{\sqrt{2}} \begin{bmatrix} 1 \\ -i \end{bmatrix}, \frac{1}{\sqrt{2}} \begin{bmatrix} 1 \\ i \end{bmatrix},$$

where all vectors are normalized to unit length.

The ellipse can be parameterized with two angles [1],

$$\tan 2\psi = \frac{2E_x(0)E_y(0)}{E_x^2(0) - E_y^2(0)} \cos \Delta\phi, \quad (1.2.3)$$

$$\sin 2\chi = \frac{2E_x(0)E_y(0)}{E_x^2(0) + E_y^2(0)} \sin \Delta\phi. \quad (1.2.4)$$

As will be shown later, ψ is the orientation of the linear polarization component and χ quantifies the amount of circular polarization component.

Jones matrices are 2×2 complex matrices that transform Jones vectors. They describe the polarization properties of optical components for monochromatic light: dichroism and birefringence, which are evaluated with diattenuation and retardance.

Dichroism is the material property that results in polarization-dependent transmission of light. The Jones matrix of a dichroic optical component with a horizontal maximum transmission is

$$\mathbf{J}_{diat} = \begin{bmatrix} T_{max} & 0 \\ 0 & T_{min} \end{bmatrix}, \quad (1.2.5)$$

where $T_{max,min}$ are the maximum and minimum flux transmittance. The component is a diattenuator if its diattenuation,

$$D = \frac{T_{max} - T_{min}}{T_{max} + T_{min}}, \quad (1.2.6)$$

is not zero. A polarizer is a diattenuator with $D = 1$, or equivalently, $T_{min} = 0$.

Birefringence is the material property that results in polarization-dependent phase change property of light. The material typically has different refractive indices along different directions.

The Jones matrix of a birefringent optical component with a horizontal fast axis (the direction of lowest refractive index) is

$$\mathbf{J}_{ret} = \begin{bmatrix} \exp(-i\delta) & 0 \\ 0 & 1 \end{bmatrix}, \quad (1.2.7)$$

where δ is the retardance. The component is a retarder if $\delta \neq 0$.

Rotation of Jones vectors in the transverse plane is described by the rotation Jones matrix

$$\mathbf{R}_{2D}(\theta) = \begin{bmatrix} \cos \theta & -\sin \theta \\ \sin \theta & \cos \theta \end{bmatrix}, \quad (1.2.8)$$

where θ is the rotation angle. In addition, a Jones matrix \mathbf{J} that is oriented θ with respect to the horizontal direction is

$$\mathbf{R}_{2D}(\theta) \cdot \mathbf{J} \cdot \mathbf{R}_{2D}(-\theta).$$

1.3 Fresnel equations

In nature, the most common sources of polarized light are refraction and reflection: Upon incidence on an interface with an abrupt change of refractive index, part of EM wave goes through the interface while the rest bounces back.

In geometrical optics, the Snell's law and the law of reflection tell where light goes after being refracted or reflected,

$$n_1 \sin \theta_i = n_2 \sin \theta_t, \quad (1.3.1)$$

$$\theta_r = -\theta_i, \quad (1.3.2)$$

where $n_{1,2}$ are the refractive indices of the materials and light incidents from n_1 's side, and $\theta_{i,t,r}$ are the incident angle, the angle of refraction and the angle of reflection. Meanwhile, physical optics studies the polarization-dependent amplitude change and phase change during refraction and reflection, which are summarized in the Fresnel coefficients. The (s, p, k) coordinate system is typically used when studying refraction and reflection, with the k coordinate aligned with the wave vector, the s coordinate perpendicular to the plane of incidence and the p coordinate within the plane of incidence (Fig. 1.1).

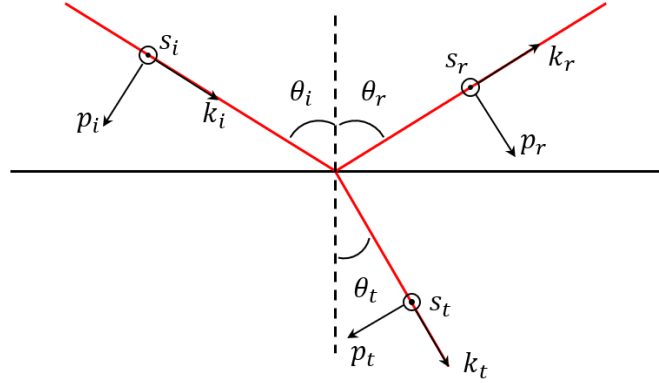


Fig. 1.1. Local coordinate systems on an interface. The subscripts i , r , and t denotes the incident light, reflected light and refracted light.

The Fresnel coefficients are

$$r_s = \frac{E_s^r}{E_s^i} = \frac{n_1 \cos \theta_i - n_2 \cos \theta_t}{n_1 \cos \theta_i + n_2 \cos \theta_t}, \quad (1.3.3)$$

$$r_p = \frac{E_p^r}{E_p^i} = \frac{2n_1 \cos \theta_i}{n_1 \cos \theta_i + n_2 \cos \theta_t}, \quad (1.3.4)$$

$$t_s = \frac{E_s^t}{E_s^i} = \frac{n_2 \cos \theta_i - n_1 \cos \theta_t}{n_2 \cos \theta_i + n_1 \cos \theta_t}, \quad (1.3.5)$$

$$t_p = \frac{E_p^t}{E_p^i} = \frac{2n_1 \cos \theta_i}{n_2 \cos \theta_i + n_1 \cos \theta_t}, \quad (1.3.6)$$

where $r_{s,p}$ and $t_{s,p}$ correspond to the reflection and refraction coefficients of light polarized in s and p directions, and $E_{s,p}^{i,r,t}$ are the s and p components of incident, reflected and refracted electric field. The Fresnel coefficients are essentially functions of three parameters: the two refractive indices and the incident angle. The flux reflectances and transmittances are related to the Fresnel coefficients as

$$R_{s,p} = |r_{s,p}|^2, \quad (1.3.7)$$

$$T_{s,p} = 1 - R_{s,p}. \quad (1.3.8)$$

When the local x coordinate is aligned with the s coordinate, the incident light is

$$\begin{bmatrix} E_s^i \\ E_p^i \end{bmatrix},$$

the transmission Jones matrix is

$$\begin{bmatrix} t_s & 0 \\ 0 & t_p \end{bmatrix}$$

and the reflection Jones matrix is

$$\begin{bmatrix} r_s & 0 \\ 0 & r_p \end{bmatrix}.$$

1.4 Stokes vectors and Mueller matrices

The polarization states of polychromatic light are typically described by Stokes vectors. Stokes vectors are 4×1 real vectors,

$$\mathbf{S} = \begin{bmatrix} S_0 \\ S_1 \\ S_2 \\ S_3 \end{bmatrix} = \begin{bmatrix} |E_x|^2 + |E_y|^2 \\ |E_x|^2 - |E_y|^2 \\ 2 \cdot \text{Re}(E_x \cdot E_y^*) \\ 2 \cdot \text{Im}(E_x \cdot E_y^*) \end{bmatrix}, \quad (1.4.1)$$

where Re , Im are functions that take the real and imaginary parts of a number, and $E_{x,y}$ are the electric field components along the local x and y coordinates. S_0 corresponds to the total flux, S_1 the horizontal/vertical linear polarization component, S_2 the $45^\circ/135^\circ$ linear polarization component, and S_3 the circular polarization component.

At a specific wavelength, a Jones vector is equivalent to the following Stokes vector [2],

$$\mathbf{S} = \mathbf{U}(\mathbf{E} \otimes \mathbf{E}^*)\mathbf{U}^{-1}, \quad (1.4.2)$$

where \mathbf{E} is the Jones vector,

$$\mathbf{U} = \frac{1}{\sqrt{2}} \begin{bmatrix} 1 & 0 & 0 & 1 \\ 1 & 0 & 0 & -1 \\ 0 & 1 & 1 & 0 \\ 0 & i & -i & 0 \end{bmatrix} \quad (1.4.3)$$

is a unitary matrix and \otimes denotes the outer product operator. Over a spectrum, a Stoke vector is equivalent to the sum of the Jones vectors over the spectrum, and it includes an extra polarization component where the polarization states at different wavelengths effectively cancel with each other. This polarization component is referred to as the unpolarized component of a Stokes

vector. Therefore, in general, there is no Jones vector that is equivalent to a Stokes vector for polychromatic light.

To quantify how much a Stokes vector is polarized, the degree of polarization (DoP) is defined as

$$DoP = \frac{\sqrt{S_1^2 + S_2^2 + S_3^2}}{S_0}. \quad (1.4.4)$$

The range of DoP is $[0, 1]$, with $DoP = 0$ describing the unpolarized state, $DoP = 1$ the fully polarized state, and all other values the partially polarized states. For monochromatic light, $DoP = 1$ as there is no unpolarized component in the Stokes vector. Similarly, the degree of linear polarization (DoLP)

$$DoLP = \frac{\sqrt{S_1^2 + S_2^2}}{S_0} \quad (1.4.5)$$

quantifies the amount of linear polarization component and the degree of circular polarization (DoCP)

$$DoCP = \frac{|S_3|}{S_0} \quad (1.4.6)$$

quantifies the amount of circular polarization component.

Stokes vectors can be studied with a unit sphere called the Poincaré sphere. The $DoP = 1$ states lie on the sphere, the DoP state is at the center of the sphere, and all other states are in between. The angle parameters ψ and χ are

$$\tan 2\psi = \frac{S_2}{S_1}, \quad (1.4.7)$$

$$\tan 2\chi = \frac{S_3}{\sqrt{S_1^2 + S_2^2}}. \quad (1.4.8)$$

Compared with a polarization ellipse, the angle parameters of a Poincaré sphere is related to the polarization state with simpler formula.

The unpolarized state, horizontal polarization state, 45° linear polarization state and right-hand circular polarization state are

$$\begin{bmatrix} 1 \\ 0 \\ 0 \\ 0 \end{bmatrix}, \begin{bmatrix} 1 \\ 1 \\ 0 \\ 0 \end{bmatrix}, \begin{bmatrix} 1 \\ 0 \\ 1 \\ 0 \end{bmatrix}, \begin{bmatrix} 1 \\ 0 \\ 0 \\ 1 \end{bmatrix}.$$

The four forms a complete set of bases for the decomposition of any Stokes vector,

$$\mathbf{S} = (1 - DoP) \begin{bmatrix} 1 \\ 0 \\ 0 \\ 0 \end{bmatrix} + DoP \begin{bmatrix} 1 \\ \cos 2\chi \cdot \cos 2\psi \\ \cos 2\chi \cdot \sin 2\psi \\ \sin 2\chi \end{bmatrix}. \quad (1.4.9)$$

Mueller matrices are 4×4 real matrices that transform Stokes vectors. They describe the polarization properties of optical components for polychromatic light: dichroism, birefringence and depolarization, which are evaluated with diattenuation, retardance and depolarization index. The first two are the same as in the case of monochromatic light. A dichroic optical component with a horizontal maximum-transmission axis is

$$\mathbf{M}_{diat} = \frac{1}{2} \begin{bmatrix} T_{max} + T_{min} & T_{max} - T_{min} & 0 & 0 \\ T_{max} - T_{min} & T_{max} + T_{min} & 0 & 0 \\ 0 & 0 & 2\sqrt{T_{max} \cdot T_{min}} & 0 \\ 0 & 0 & 0 & 2\sqrt{T_{max} \cdot T_{min}} \end{bmatrix}, \quad (1.4.10)$$

where $T_{max,min}$ are the maximum and minimum flux transmittance. A birefringent optical component with a horizontal fast axis is

$$\mathbf{M}_{ret} = \begin{bmatrix} 1 & 0 & 0 & 0 \\ 0 & 1 & 0 & 0 \\ 0 & 0 & \cos \delta & \sin \delta \\ 0 & 0 & -\sin \delta & \cos \delta \end{bmatrix}, \quad (1.4.11)$$

where δ is the retardance. Rotation of Stokes vectors in transverse plane is described by the rotation Mueller matrix,

$$\mathbf{R}_{2D}(\theta) = \begin{bmatrix} 1 & 0 & 0 & 0 \\ 0 & \cos 2\theta & -\sin 2\theta & 0 \\ 0 & \sin 2\theta & \cos 2\theta & 0 \\ 0 & 0 & 0 & 1 \end{bmatrix}, \quad (1.4.12)$$

where θ is the rotation angle. In addition, a Mueller matrix \mathbf{M} that is oriented θ with respect to the horizontal axis is

$$\mathbf{R}_{2D}(\theta) \cdot \mathbf{M} \cdot \mathbf{R}_{2D}(-\theta).$$

Depolarization is the material property that results in a decrease of DoP. It originates from the incoherent addition of different polarization states of light. A fully depolarizing Mueller matrix transform any incoming polarization state to the unpolarized state,

$$\mathbf{M}_{depol} = \begin{bmatrix} 1 & 0 & 0 & 0 \\ 0 & 0 & 0 & 0 \\ 0 & 0 & 0 & 0 \\ 0 & 0 & 0 & 0 \end{bmatrix}. \quad (1.4.13)$$

The depolarization index (DI) quantifies the ability of depolarizing light by measuring the distance between the normalized Mueller matrix and the identity matrix,

$$DI = \left\| \frac{\mathbf{M}}{m_{0,0}} - \mathbf{I} \right\| = \frac{\sqrt{(\sum_{i,j} m_{i,j}^2) - m_{0,0}^2}}{\sqrt{3}m_{0,0}}, \quad (1.4.14)$$

where \mathbf{I} is the 4×4 identity matrix and $m_{i,j}$ is the matrix element of \mathbf{M} in the i 'th row and j 'th column. A fully depolarizing Mueller matrix has a DI of 1 and a non-depolarizing Mueller matrix has a DI of 0.

1.5 Transmission and reflection Mueller matrices

When the local x coordinate is aligned with the s coordinate, the transmission Mueller matrix is

$$\mathbf{T} = \frac{1}{2} \begin{bmatrix} T_s + T_p & T_s - T_p & 0 & 0 \\ T_s - T_p & T_s + T_p & 0 & 0 \\ 0 & 0 & 2\sqrt{T_s \cdot T_p} & 0 \\ 0 & 0 & 0 & 2\sqrt{T_s \cdot T_p} \end{bmatrix}, \quad (1.5.1)$$

and the reflection Mueller matrix is

$$\mathbf{R} = \frac{1}{2} \begin{bmatrix} R_s + R_p & R_s - R_p & 0 & 0 \\ R_s - R_p & R_s + R_p & 0 & 0 \\ 0 & 0 & -2\sqrt{R_s \cdot R_p} & 0 \\ 0 & 0 & 0 & -2\sqrt{R_s \cdot R_p} \end{bmatrix}. \quad (1.5.2)$$

Note that the extra minus sign in the two diagonal terms in the reflection Mueller matrix results from the change of local coordinates upon reflection.

Chapter 2. Polarization-based image separation with unpolarized objects

2.1 Background

In conventional imaging, the objects of interest are those inside the camera's field of view (FoV) that emit or reflect photons. There are two major types of reflection: specular reflection and diffuse reflection (i.e. scattering). The photons of interest collected from a reflecting object in conventional imaging are the primarily diffuse reflection photons (or direct photons), and due to the little amount of spatial modulation information they have about the illumination source (typically at certain distance away from the object), these photons are typically treated the same as emitted photons from the object. Compared with specular reflection photons, they contain a wider angular spectrum of the irradiance modulation of the object's surface. Meanwhile, specular reflection preserves the spatial modulation information of the illumination source. A specular reflection photon (or an indirect photon) may undergo multiple times of bounces and follow an indirect pathway to the camera. The separation of indirect photons from the direct photons can provide valuable information of hidden objects that are outside the FoV, which are invisible in conventional imaging.

Image separation is the study of the techniques that separate overlapping information inside the FoV. The input is one or more images of a scene, and the output is two or more images that contain separated pieces of information. Furthermore, each piece of information (individual image) is typically assumed to have certain known relation with others, either uncorrelated (e.g. reflection and transmission on a glass window) or fully correlated (e.g. different orders of ghost reflections on a glass window). The separation of direct photons and indirect photons, when the

photons have spatial modulation, belong to image separation. The separation of photons will be the focus of this dissertation, and we will refer to it as image separation.

Image separation can be performed with little, partial, or full prior information of the objects of interest and reflected surfaces with decreasing difficulty. When there is little prior information, blind separation methods such as the independent component analysis (ICA) [3] are typically employed. ICA has been successfully applied to audio signal separation in the so-called ‘cocktail party’ problem [4-6], image separation problems such as astrophysical component separation [7], electroencephalographic data collection [8] as well as for feature extraction and noise removal. The robustness of blind separation methods is highly dependent on the correlation of the components, and their performance are thus limited by the inherent noise in the different components [9, 10]. Other relevant separation methods include user-assisted separation [11], reflection removal using ghosting cues [12] and machine learning [13]. On the other hand, when partial prior information is available, the fidelity of separation can often be improved by exploiting a physical model of the scene [14, 15]. Existing methods use the polarization effect on the reflecting light and assume a prior knowledge of the medium of the reflection surface to calculate the reflectance and transmittance. This knowledge includes the surface being flat and uniform, and statistical independence of transmitting and reflecting object (referred to as object T and object R in this dissertation) [14, 15]. The surface flatness and uniformity requirements are typically satisfied in scenarios where the reflections are from a window or from a floor. The requirement on statistical independence cannot be generally applied to all scenes, for example, the separation of objects that are similar in shape and intensity. Aside from acquiring a higher fidelity, the separation with prior information typically requires less time to perform, too.

The most complete prior information of a scene is its light field function, which is a function of space, angle, time, wavelength, polarization and coherence. These days, a commercial camera is typically designed for and performs the best at capturing spatial, temporal, and, to a lesser extent, spectral information. The capture of angular information often requires capturing the same scene at multiple view points, and it can be incorporated into image separation [16]. This method does not necessarily require additional devices other than a commercial camera and it performs well in most cases (when different objects are at different distances away from the camera), while the computation is typically time-consuming. Meanwhile, the capture of coherence information is typically done through interferometry, which cannot be easily incorporated into imaging [17]. Quantifying the decoherence property of a surface is also not easy. Therefore, we rarely see the use of coherence information in image separation.

The capture of polarization information requires an imaging polarimeter, which can be as simple as a commercial camera and a linear polarizer. Direct measurement of polarization images, which can include all or partial components of the Stokes vector, can be measured in real-time by using a linear-Stokes or a full-Stokes imaging polarimeter [18-20]. As specular reflection induces polarization change in light, it is also natural to incorporate the polarization information into image separation. Advantages of this technique include (1) good separation for a variety of scenes, (2) separation of both black and white and color images, (3) applicability to reflection from transparent or opaque semi-glossy objects, and (4) ability to estimate surface reflection angle, i.e. 3D information about the reflector. Disadvantages are (1) low fidelity when the incident angle on the reflector is small, and (2) requirement of polarization optics elements.

2.2 Mueller matrix equations for image separation with unpolarized objects

In this chapter, we consider the case where the objects of interest emit or reflect unpolarized light. This is true for most emission (e.g. from the sun, lamps and light-emitting diodes) and for scattering (e.g. from grass, soil), but not true for objects like liquid crystal displays and metal/plastic parts. We will consider the latter cases in the next chapter. The Stokes vector of unpolarized light is $S_0[1,0,0,0]^T$, where S_0 is the irradiance and T denotes the transpose operation. In general, S_0 is a function of space and time, while we acknowledge this throughout this dissertation and thus will not explicitly write it out.

Two widely-seen semi-reflective surfaces are transparent windows and glossy opaque surfaces. Transparent windows consist of two parallel surfaces and transmits/reflects light; therefore, it can be modeled similarly to a typical interface using the transmission and reflection Mueller matrices. Meanwhile, glossy opaque surfaces are of various types, for example, glossy printer paper, painted wall and marble surface. An uncoated surface (e.g. marble tile surface) can be modeled as the combination of an interface and an underlying scattering object, while a coated surface (e.g. glossy printer paper surface) as that of a transparent window and an underlying scattering object. Note that this simplification does not consider interferometric or plasmonic effects, so surfaces or coatings like gratings, optical thin films, meta-surfaces or 2D photonic crystals is not included in this study. Since these elements are designed to be used in either transmission or reflection mode, the overlapping is typically minimal; still, when used not under their designed conditions, there could be situations that worth further study.

A schematic of the scene when the reflector is a transparent window is as below (Fig. 2.1). The incident angle of the rays from the two objects are ϕ , and the rotation angle from the reflector's local coordinate to the camera's local coordinates is θ .

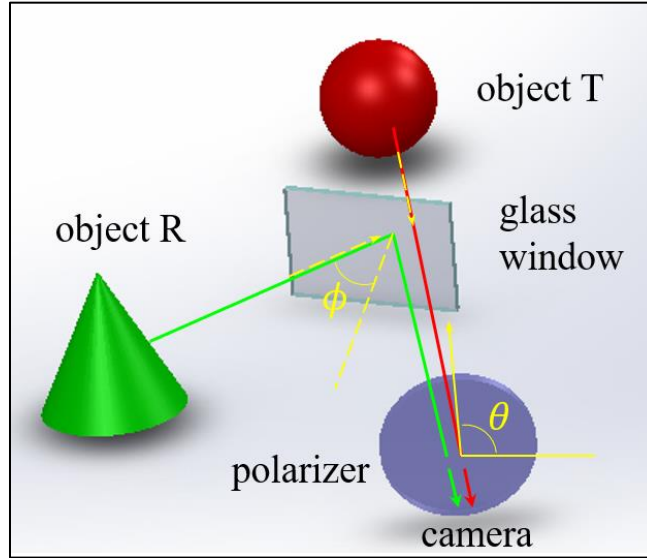


Fig. 2.1 Schematic of the scene. Modified from ref. [21].

Inside a transparent window, there are multiple reflections of rays in between the two parallel surfaces. We assume that the camera is at a distance from the window so that multiple reflections overlap with each other when captured by the camera. This is true for a thin window, while a thick window or a close distance results in ghost reflections [12, 22]. In addition, we assume that the material of the window is not absorbing, which applies to most glass materials used in everyday life. The reflection Mueller matrix is

$$\mathbf{R}^w(\phi) = \frac{1}{2} \begin{bmatrix} R_s^w(\phi) + R_p^w(\phi) & R_s^w(\phi) - R_p^w(\phi) & 0 & 0 \\ R_s^w(\phi) - R_p^w(\phi) & R_s^w(\phi) + R_p^w(\phi) & 0 & 0 \\ 0 & 0 & R_{33}^w(\phi) & 0 \\ 0 & 0 & 0 & R_{33}^w(\phi) \end{bmatrix}, \quad (2.2.1)$$

where

$$R_{33}^w(\phi) = \sqrt{\frac{R_s^w(\phi)R_p^w(\phi)}{(2 - R_s^w(\phi))(2 - R_p^w(\phi))}} \cdot \frac{3R_s^w(\phi) + 3R_p^w(\phi) - 2R_s^w(\phi)R_p^w(\phi) - 4}{2 - R_s^w(\phi) - R_p^w(\phi)}, \quad (2.2.2)$$

and

$$R_{s,p}^w(\phi) = \frac{2R_{s,p}(\phi)}{1 + R_{s,p}(\phi)}. \quad (2.2.3)$$

The transmission Mueller matrix is

$$\mathbf{T}^w(\phi) = \frac{1}{2} \begin{bmatrix} T_s^w(\phi) + T_p^w(\phi) & T_s^w(\phi) - T_p^w(\phi) & 0 & 0 \\ T_s^w(\phi) - T_p^w(\phi) & T_s^w(\phi) + T_p^w(\phi) & 0 & 0 \\ 0 & 0 & T_{33}^w(\phi) & 0 \\ 0 & 0 & 0 & T_{33}^w(\phi) \end{bmatrix}, \quad (2.2.4)$$

where

$$T_{33}^w = \frac{4T_s^w(\phi)T_p^w(\phi)}{T_s^w(\phi) + T_p^w(\phi)}, \quad (2.2.5)$$

and

$$T_{s,p}^w(\phi) = 1 - R_{s,p}^w(\phi). \quad (2.2.6)$$

We will refer to the two as the window reflection/transmission Mueller matrices. The reader may refer to ref. [21] for detailed derivation. Let $\mathbf{S}^{Tr} = S_0^{Tr}(1,0,0,0)^T$ and $\mathbf{S}^{Re} = S_0^{Re}(1,0,0,0)^T$ be the Stokes vectors of object T and object R, and the Mueller matrix equation is

$$\mathbf{S}^{cam} = \mathbf{R}_{2D}(\theta)(\mathbf{T}^w(\phi)\mathbf{S}^{Tr} + \mathbf{R}^w(\phi)\mathbf{S}^{Re}), \quad (2.2.7)$$

where \mathbf{S}^{cam} is the Stokes vector at the camera and $\mathbf{R}_{2D}(\theta)$ is the rotation matrix from the reflector's local coordinate to the camera's local coordinate. Substituting the components of the Stokes vectors of the objects into the equation gives,

$$\mathbf{S}^{cam} = \frac{1}{2} \begin{bmatrix} (T_s^w(\phi) + T_p^w(\phi)) S_0^{Tr} + (R_s^w(\phi) + R_p^w(\phi)) S_0^{Re} \\ \cos 2\theta (R_s^w(\phi) - R_p^w(\phi)) (S_0^{Re} - S_0^{Tr}) \\ \sin 2\theta (R_s^w(\phi) - R_p^w(\phi)) (S_0^{Re} - S_0^{Tr}) \\ 0 \end{bmatrix}. \quad (2.2.8)$$

When the transmitted (reflected) light is normal incident to the reflector, or when object T is as bright as object R, the captured light is unpolarized and the separation cannot be done. In the former case, object R is the camera itself, and is typically not of interest. In addition, the latter case should happen only at a limited number of pixel locations for object T and object R to be distinguishable, and the error there will not affect other pixels. Therefore, it is natural that we do not consider these two cases, and

$$\theta = \frac{1}{2} \tan^{-1} \left(\frac{S_2^{cam}}{S_1^{cam}} \right). \quad (2.2.9)$$

Note that modern software programs generally take in $S_{1,2}^{cam}$ and calculate θ without performing the division, so there is no error when $\theta = \pm 90^\circ$. After θ is calculated,

$$S_0^{Tr,Re}(\phi) = S_0^{cam} - \frac{S_1^{cam}}{\cos 2\theta \cdot D^{Re,Tr}(\phi)}, \quad (2.2.10)$$

where

$$D^{Tr}(\phi) = \frac{T_s^w(\phi) - T_p^w(\phi)}{T_s^w(\phi) + T_p^w(\phi)}, \quad (2.2.11)$$

and

$$D^{Re}(\phi) = \frac{R_s^w(\phi) - R_p^w(\phi)}{R_s^w(\phi) + R_p^w(\phi)}. \quad (2.2.12)$$

The $D^{Tr,Re}(\phi)$ terms are the diattenuation of transmission and reflection. Note that the superscript of $D^{Re,Tr}(\phi)$ has a reverse order of the superscript of $S_0^{Tr,Re}(\phi)$, for the computation of $S_0^{Tr}(\phi)$ involves removing $S_0^{Re}(\phi)$ from S_0^{cam} , and vice versa.

For an uncoated surface (e.g. marble surface), we use the reflection Mueller matrix from chapter 1 to model the specular reflection at the air-material interface and an unpolarized Stokes vector for the volume scattering component from inside the material. The latter component then transmits through the surface of the material, so the transmission Mueller matrix is considered.

The Mueller matrix equation is

$$\mathbf{S}^{cam} = \mathbf{R}_{2D}(\theta)(\mathbf{T}(\phi)\mathbf{S}^{Sc} + \mathbf{R}(\phi)\mathbf{S}^{Re}), \quad (2.2.13)$$

where \mathbf{S}^{Sc} denotes the Stokes vector of volume scattering. Substituting $\mathbf{T}^W(\phi)$ with $\mathbf{T}(\phi)$ and $\mathbf{R}^W(\phi)$ with $\mathbf{R}(\phi)$ in the solution to the transparent window case, the solution to $S_0^{Sc,Re}$ is

$$S_0^{Sc,Re}(\phi) = S_0^{cam} - \frac{S_1^{cam}}{\cos 2\theta \cdot D^{Re,Tr}(\phi)}, \quad (2.2.14)$$

where

$$D^{Tr}(\phi) = \frac{T_s(\phi) - T_p(\phi)}{T_s(\phi) + T_p(\phi)}, \quad (2.2.15)$$

and

$$D^{Re}(\phi) = \frac{R_s(\phi) - R_p(\phi)}{R_s(\phi) + R_p(\phi)}. \quad (2.2.16)$$

Note that \mathbf{S}^{Sc} contains both the spatial information of illumination and that of the reflector's material, so only when the illumination source is far away from the reflector can \mathbf{S}^{Sc} be approximated as the spatial scattering property of the reflector.

For a coated surface (e.g. glossy printer paper surface), we use the window reflection Mueller matrix to model the specular reflection on the coating and an unpolarized Stokes vector for the volume scattering component from inside the substrate. The Mueller matrix equation is

$$\mathbf{S}^{cam} = \mathbf{R}_{2D}(\theta)(\mathbf{T}^W(\phi)\mathbf{S}^{Sc} + \mathbf{R}^W(\phi)\mathbf{S}^{Re}), \quad (2.2.17)$$

and the solution to $S_0^{Sc,Re}$ is

$$S_0^{Sc,Re}(\phi) = S_0^{cam} - \frac{S_1^{cam}}{\cos 2\theta \cdot D^{Re,Tr}(\phi)}, \quad (2.2.18)$$

where $D^{Tr,Re}(\phi)$ are the same as in the transparent window case.

2.3 Evaluation of image correlation

The correct incident angle ϕ is necessary to solve for $S_0^{Tr,Re,Sc}(\phi)$. If ϕ can be measured, then the separation problem is solved. However, this piece of information is typically unknown and requires estimation for (but not limited to) the following reasons: (1) the reflector may be far away from the camera, and (2) fast separation is needed while measuring the incident angle becomes the bottleneck. To estimate ϕ , the separation can be performed for a series of N possible ϕ values, then the optimal ϕ value, ϕ_{opt} , can be determined with image analysis of the $2N$ separated images. By definition, the optimal separation results in the least residual on both

separated images. With computer algorithms, the optimal separation gives the least similar separated images for a given incident angle if object T and R are statistically uncorrelated, i.e. look different, and the least change in a separate image against the variation of incident angle (i.e. the variation of residual is stable at ϕ_{opt}). We explore the first property of ϕ_{opt} in this dissertation, while the second one is also worthy of studying.

One popular image correlation metric is the cross-correlation. It is based on a pixel-wise comparison of images that capture different sub-regions of the same object [23, 24] and has been applied to estimate image shifts and distortion. Meanwhile, mutual information (MI) is based on image statistics and is applied to evaluate two overlapping grayscale images [14],

$$MI(\phi) = \sum_{hist} P(I_1, I_2) \log \left(\frac{P(I_1, I_2)}{P(I_1)P(I_2)} \right), \quad (2.3.1)$$

where P in $MI(\phi)$ denotes the probability of observing a specific grayscale value in the histogram of an image or images. The MI metric evaluates the statistical similarity (or distance) between two statistical distributions (histograms) defined on the irradiances of the two objects. A third metric function, which we defined specifically for the image separation problem, is a variation of the cross-correlation and is defined based on the edge map of the two separated images. Edge information is well-known in both image analysis and image understanding and it encodes significant symbolic information about the scene. For example, for a band limited image which is irreducible as polynomial, it is possible to fully reconstruct the image only given the edge information [25]. We define the edge overlap (EO) cross correlation metric, evaluated on each of the RGB color channels separately, to equal the number of pixels at the same location where both images have an edge present,

$$EO(\phi) = \sum_{i,j} \Delta_{ij}(I_1) \Delta_{ij}(I_2), \quad (2.3.2)$$

and Δ_{ij} takes on the value 1 if there is an edge and 0 if no edge is detected at the pixel location (i, j). For the edge detection itself, we apply the Canny edge detector [26-29] with an optimized threshold that minimizes the number of false edges.

Minimizing the metric for each color (i.e. RGB) channel yields an incident angle estimate $\phi_{opt} = \arg \min EO(\phi)$, which is then used to recover the separate image for each color. The consistency of the incident angle estimated across different color channels. For simplicity, we chose a limit of 10° as the maximum acceptable incident angle difference across RGB channels. If ϕ_{opt} across all three channels are within 10° of each other, the three values are averaged to yield a single final incident angle estimate; otherwise, the incident angle estimation is inconsistent, and the separation is treated as unsuccessful.

2.4 Separation algorithm

The separation algorithm consists of four major steps. First, capturing images with an imaging polarimeter and computing \mathcal{S}^{cam} with data reduction. Secondly, performing image separation for a series of possible incident angle values. Thirdly, estimating the incident angle. Finally, recovering the correct separated object T and R images with ϕ_{opt} . A block diagram is shown below (Fig. 2.2).

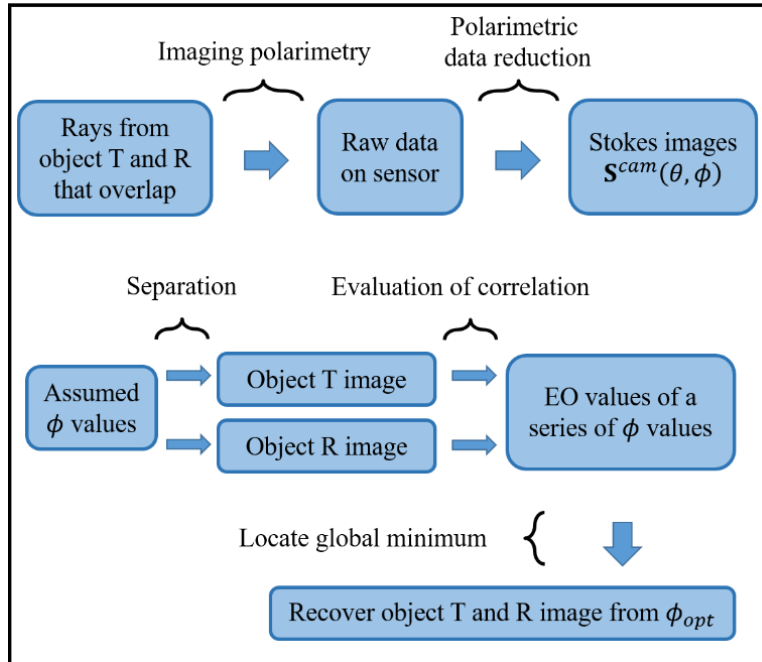


Fig. 2.2. Separation algorithm. (a) A block diagram shows the calculation of transmitted and reflected Stokes images from data taken by imaging polarimetry. (b) The separation of light from object T and object R is performed by finding ϕ that minimizes the metric function. Modified from ref. [21].

2.5 Collection of separation results

A variety of scenes were studied in our experiments, both indoor and outdoor and both in the visible and in the infrared spectrum. For the indoor scenes in the visible spectrum, we illuminated the object T and R with an incandescent lamp (5500K, 900 lumens) and a pico-projector, respectively. The pico-projector, Model AAXA P2 Jr., was operated under low brightness mode to project a 5500 K uniform white image. For the indoor scenes in the infrared spectrum, the illumination sources were an infrared light bulb (RubyLux NIR-A infrared bulb)

and a StudioPRO standard 45W photo fluorescent spiral daylight light bulb. For the outdoor scenes, the illumination sources were the sun and the fluorescent lamps inside the building.

Static images in the visible spectrum were acquired using a Sony DSLR-A350 camera with a Sigma 17-35 mm aspherical lens. A linear polarizer (HOYA 72 mm linear polarizing filter) were placed in front of the camera and rotated manually to measure different polarization states. Static images in the long wave infrared spectrum were taken using a Seek Thermal CompactPRO thermal camera. A ZnSe based linear polarizer (THORLABS WP50H-Z holographic wire grid polarizer) was used in front of the camera and was rotated manually for different measurements.

Videos in the near infrared were taken using a customized IMPERX ICL-B1620W-KC000 CCD camera with combination of a zoom lens (Computar H6Z0812 C-Mount) and a close-up lens (Vivitar 49 mm close-up lens). A 760 nm bandpass filter and a micro polarizer array of 2×2 elliptical micro polarizers[30] were mounted in front of the CCD sensor to form a full-Stokes division of focal plane imaging polarimeter[31]. Resolution of the polarimeter was $1608 \times 1208 \times 14$ bit, and the frame rate was 12 frames per second. Video in the visible spectrum was taken by a commercial PolarCam camera from 4D Technology using the same lens system as the near infrared. This division of focal plane imaging polarimeter utilized linear wire grid micro-polarizer and had a resolution of $2400 \times 1800 \times 16$ bit and a frame rate of 18 frames per second. The calibration of the cameras and computation of the Stokes images are described in reference[31].

We tested the image separation method for a variety of reflectors. For the indoor scenes, we considered a glass from a common photo frame as the reflector. Object T and object R were illuminated individually. We assumed that the glass is BK7 glass ($n = 1.52$). While the

dispersion effect between RGB channels can be included, our calculation indicates that the reflectance change is smaller than 3.5% in the visible range (400 – 700 nm). The measured incident angle is 61.9° . Minimizing EO yields incident angles of 62° , 67° and 66° for RGB channels. Residual exists in the separated images, especially in the separated object R image. We attribute the residual in part to the underestimation of the refractive index.

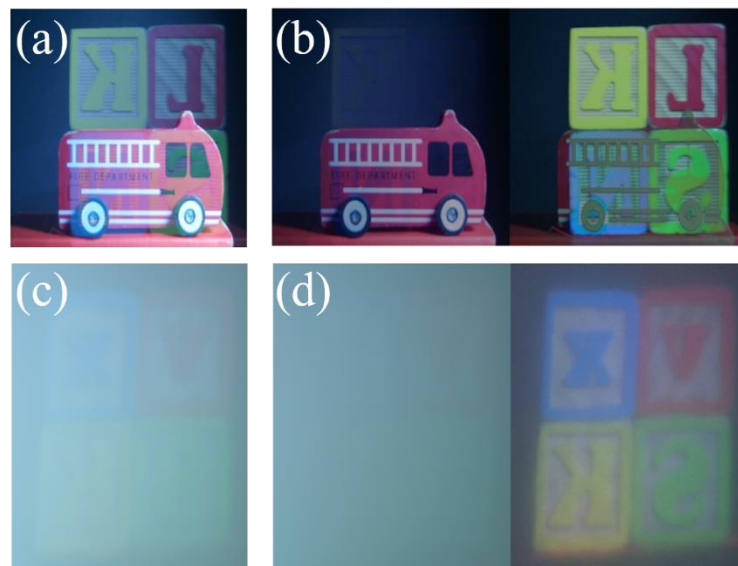


Fig. 2.3. Separation of indoor scenes. (a) An overlapping indoor scene consisting of a toy car, four letter blocks and a piece of glass with an incident angle of 61.9° . (b) The separated object T and object R images are shown for the EO metric function. (c) An indoor scene consisting of four letter blocks and a piece of glossy printer paper with an incident angle of 53.1° . (d) The separated object T and object R images are shown for the EO metric function [21].

Next, we quantified the fidelity of the separated images using reference individual images of the objects T and R that were taken separately. The individual image of object T (object R) was taken with the two illumination sources on and a black scattering cardboard inserted between

object R (object T) and the glass window. We employed the median absolute deviation (MAD) metric for normalized images to quantify the fidelity of the separated images. Compared with the mean squared error (MSE), MAD is more resilient to outliers in an image and thus is more robust. The mathematical form of the MAD measured in our experiments is $MAD = \frac{1}{3} \sum_{r,g,b} \sum_{pixel} |\bar{S}_{0;r,g,b}^{exp} - \bar{S}_{0;r,g,b}^{ref}|$, where $\bar{S}_{0;r,g,b}^{exp,ref}$ denotes the irradiances of the separated/reference image after linear normalization to a new dynamic range of (0,1). The result of MAD is summarized in Table 3.1.

We then replaced the glass surface by a glossy printer paper for an indoor diffuse surface separation experiment. For this experiment, the scene was illuminated with a single source. This results in a slightly polarized incident light onto the coating-paper surface; nevertheless, our technique provides good separation of object R. Coated paper has an effective refractive index around 1.3 [32]. The measured incident angle for this scene is 53.1° . Minimizing the EO metric yields incident angle estimates of 55° , 54° and 54° (RGB), which is close to the measured value. To evaluate the separated image fidelity, we inserted a cardboard between the color blocks and the glossy paper and took the individual image of the surface as the reference image. Under this configuration, the paper was weakly yet uniformly illuminated by the ambient light.

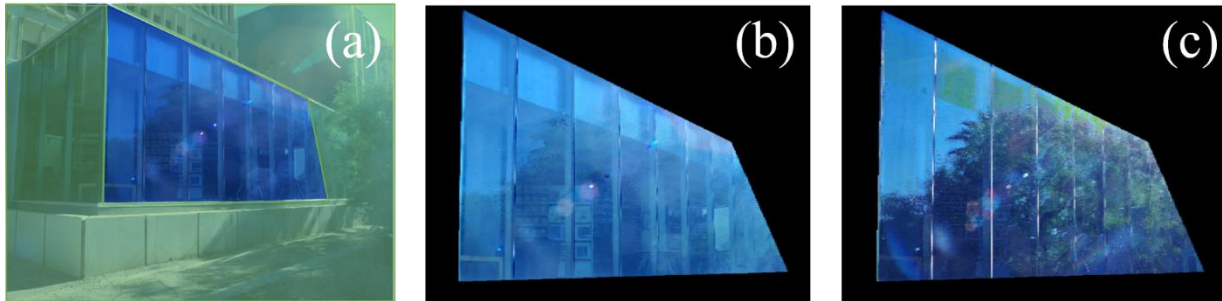


Fig. 2.4. Patch-wise separation of trees from a window. (a) A polygon shape (green) is used to mask the window in the input image. Only the unmasked part is considered in the incident angle estimation. Separation result by minimizing the EO metric function is shown in (b) and (c) [21].

Our outdoor scene is centered on large glass window panes of a library situated next to a cluster of trees. Because the window panes are the only region of interest, the raw image is masked to eliminate other parts of the scene and thus, it is not included in the metric evaluation [Fig. 2.4(a)]. As the size of the trees is comparable to their-distance to the camera, we employ a patch-wise separation approach. Note that the accuracy of incident angle estimate reduces for patches that contain the masked area due to fewer sampling points. For each patch, we compute the incident angle estimate using the same approach as the indoor scene separation. We fit a second order polynomial to the incident angle estimates of different patches and obtain a smooth map of incident angles across the entire scene. Compared with non-patch-wise separation approach, the incident angles estimated using the EO metric are close to the actual incident angles from physical measurements; the average incident angle deviation using patch-wise separation is 5.1° . Thus, the patch-wise separation provides a more accurate representation of the outdoor scene.

A hallway scene with glossy floor was chosen for our surface separation experiment in the visible spectrum. The floor acts as an uncoated surface with a refractive index of 1.65 [33]. The measured incident angle for the exit sign is 52.7° while minimizing the EO metric yields 52° , 54° , 53° (RGB). The measured incident angle for the fluorescent lamp is 51.1° and we obtain 52° , 53° , 52° (RGB) incident angle estimates by minimizing EO. To evaluate fidelity of the separated images, we assumed that the specific area of the floor is black and uniform in color. Results from the incident angle estimation and MAD show that separation obtained using the EO metric is close to the actual physical scene.

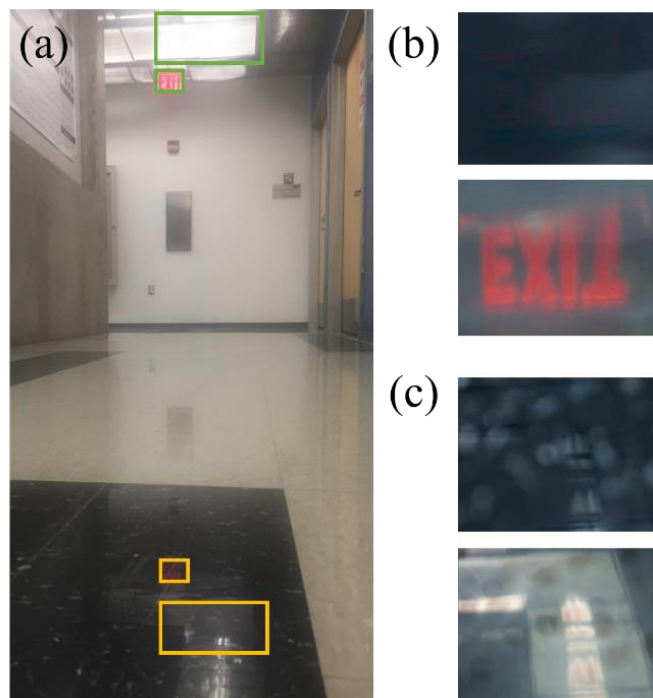


Fig. 2.5. A hallway scene consisting of fluorescent lights, an exit sign on the ceiling, and glossy floor. (a) The scene, with object Rs in green boxes and their reflection in yellow boxes. (b) Separation of exit sign from glossy floor by minimizing the EO metric function. (c) Separation of light from glossy floor by minimizing the EO metric function.

We also performed an experiment in the long-wave infrared (LWIR) spectral band, where the object acts as the source of radiation. The scene consists of a glass plate in front of a paper-made ‘OSC’ pattern as the object T and an incandescent light bulb as the object R. The paper is heated by another incandescent bulb placed behind the glass plate, providing a thermal patterned background. The goal of this experiment is to separate the thermal pattern of the object R from the background thermal pattern of the object T. We adjusted the glass plate orientation to setup three different incident angles at 48° , 60° and 66° . The actual angles ϕ_{meas} are measured from the scene and compared with the angles estimated using the EO method. In all three angles, the EO method provides a close estimation.

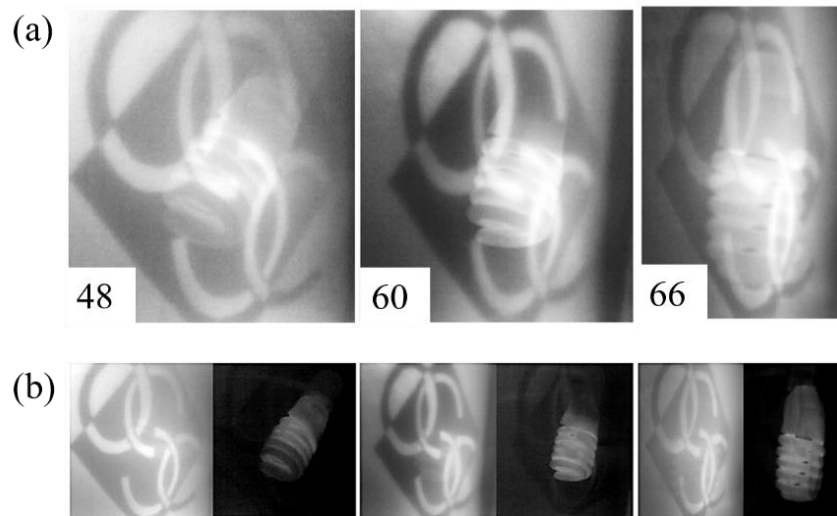


Fig. 2.6. Comparison of the separation results for different incident angles. (a) Overlapping images for incident angles of 48° , 60° and 66° . (b) The separated images using the EO method.

For glossy surfaces in the LWIR spectrum, the separation experiments were performed using two types of reflector surface, a glossy paper surface and a white paint surface on dry wall

(BEHR Premium Plus Ultra Pure White Eggshell Zero VOC Interior Paint) in the LWIR spectrum. The surfaces were chosen for their different diffuse and specular reflection components. The object R consists of a halogen lamp behind a paper mask in the shape of the letter A, the logo for the University of Arizona, and the incident angle is fixed at 76° . Figure 2.7 shows the results of the image separation.

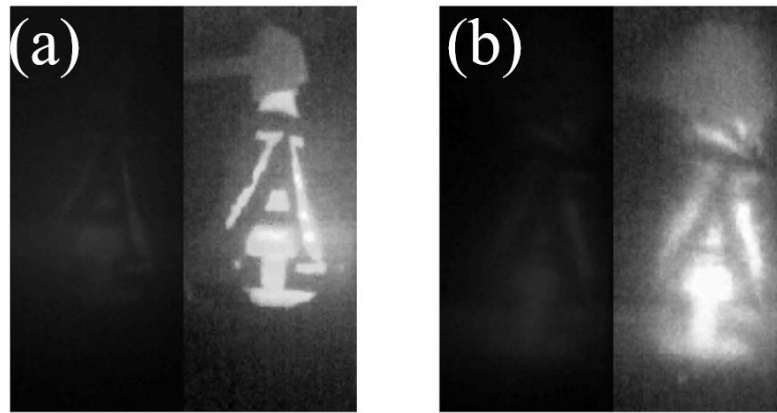


Fig. 2.7. Separation with diffuse surfaces. (a) Separated images from reflection of a glossy paper calculated using EO as the metric function. (b) Separated images from reflection of a white paint surface calculated using EO as the metric function.

Table 3.1. MAD of the indoor and outdoor scenes using the EO methods.

Indoor transparent (object T)	Indoor transparent (object R)	Indoor glossy (object T)	Outdoor glossy (object T)
0.0395	0.1290	0.0427	0.3047

2.6 The SNR limit of separation

The fidelity of separation is limited by the signal-to-noise ratio (SNR), where the signal is the polarized reflected light from specular reflection (SR) on the reflector's surface, and the noise is the unpolarized reflected light from surface scattering or volume scattering (uniform diffuse reflection, or UDR). Reflection from a flat surface, such as a glass window, obeys the law of reflection, where the incident angle is equal to the angle of reflection. Meanwhile, for glossy surfaces, the reflected energy, I_R , is made up of a polarized SR component, I_{SR} , and an unpolarized UDR component, I_{UDR} . In general, I_{SR} has both s and p polarized light, and the modulation depth is given by $(I_s - I_p)/2$, which is close to a cosine square wave as a function of the polarizer's angle per Malus' law. I_{UDR} can be considered generally uncorrelated or weakly dependent on I_{SR} and therefore can be treated here as a source of background noise in the calculation of the reflected image. The reflected energy in diffuse reflection is assumed to be proportional to the incident energy, I_{inc} , by a constant factor α , i.e. $I_{UDR} = \alpha I_{inc}$. The s and p polarized components of I_{SR} is a function of the reflectances, $R_{s,p}^W$, and I_{inc} . The SNR and SR component in the coated surface case are given by

$$SNR = \frac{I_s - I_p}{2 \cdot I_{UDR}} = \frac{(R_s^W - R_p^W)(1 - \alpha)}{2\alpha}, \quad (2.6.1)$$

$$\frac{I_{SR}}{I_R} = \frac{(R_s^W - R_p^W)(1 - \alpha)}{(R_s^W + R_p^W)(1 - \alpha) + 2\alpha}. \quad (2.6.2)$$

As SNR is a function of the refractive index of the reflector and the ratio I_{SR}/I_R , in general, reflectors with a higher refractive index have a higher polarization modulation and SNR. Alternatively, reflectors with a higher scattering have a lower SNR.

Figure 2.8 shows the relationship between SNR and I_{SR}/I_R . SNR is a monotonically decreasing function of I_{SR}/I_R . Paper coating has a larger refractive index in LWIR than white paint, leading to a higher SNR. The refractive indices for the paper coating and white paint are calculated from data in [34] and [35] for the wave number range of $700\text{--}1400\text{ cm}^{-1}$ ($7\text{--}14\text{ }\mu\text{m}$), which is the nominal detectable range of the LWIR camera. For precipitated calcium carbonate (PCC) which makes up the paper coating, the refractive index is calculated by first averaging the reflectances over o-ray and e-ray assuming that the calcite particulates are randomly orientated. This assumption is also applied to the TiO_2 particulates in the white paint in which the reflectances along and perpendicular to the c-axis are averaged. The measured values for I_{SR}/I_R for the two materials are also plotted on the two curves. The SNR for image separation with the glossy paper (white paint) as a reflector is estimated to be 3.4 (0.56) respectively.

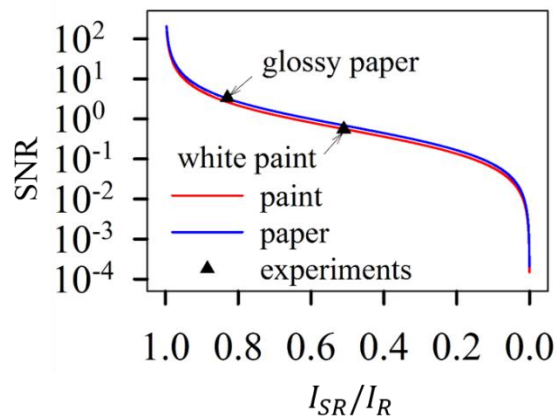


Fig. 2.8. SNR for reflectors that have both specular and diffuse components in LWIR. The SNR is plotted as a function of I_{SR}/I_R for glossy paper ($n = 1.77$) and white paint ($n = 1.50$). Modified from ref. [21].

2.7 Image separation in the scenes with multiple reflectors

The image separation method above can be extended to use in the scenes with more than one reflector under certain conditions. In the case of two reflectors where light reflects on reflector 1 and then reflector 2 and is then detected by the camera, the Mueller matrix equation set is

$$\mathbf{S}^{cam} = \mathbf{R}_{2D}^{2 \rightarrow cam}(\theta_2)(\mathbf{T}(\phi_2)\mathbf{S}_2^{Tr} + \mathbf{R}(\phi_2)\mathbf{S}_2^{Re}), \quad (2.7.1)$$

$$\mathbf{S}_2^{Re} = \mathbf{R}_{2D}^{1 \rightarrow 2}(\theta_1)(\mathbf{T}(\phi_1)\mathbf{S}_1^{Tr} + \mathbf{R}(\phi_1)\mathbf{S}_1^{Re}), \quad (2.7.2)$$

where $\mathbf{R}_{2D}^{2 \rightarrow cam}(\theta_2)$ and $\mathbf{R}_{2D}^{1 \rightarrow 2}(\theta_1)$ are the rotation Mueller matrices from reflector 2 to the camera and from reflector 1 to reflector 2, $\theta_{1,2}$ are the orientations of reflector 1 and 2, $\phi_{1,2}$ are the incident angles on reflector 1 and 2, and $\mathbf{S}_{1,2}^{Tr,Re}$ are the Stokes vectors of object T's and object R's. To solve this equation set, the second equation can be substituted into the first equation, which results in a vector equation that consists of three scalar equations and seven unknowns (four angle parameters and three irradiances of the images). Though we can assume the statistical independence of images as in the case of one reflector, which gives three equations of minimizing the correlation between \mathbf{S}_1^{Tr} and \mathbf{S}_2^{Tr} , \mathbf{S}_1^{Re} and \mathbf{S}_2^{Re} and \mathbf{S}_1^{Tr} and \mathbf{S}_1^{Re} , we have seven knowns and six equations and the equation set is not solvable.

To study when the separation algorithm in previous sections can be extended, the number of unknowns and the number of scalar equations are studied as functions of the number of reflectors. Adding a reflector adds in four unknowns (two angle parameters and three Stokes images) and one vector equation. This additional vector equation can be substituted into the existing vector equation, which eliminates one Stokes image (e.g. \mathbf{S}_2^{Re}) and leaves two Stokes images to describe unpolarized light (e.g. \mathbf{S}_1^{Tr} and \mathbf{S}_1^{Re}). Meanwhile, a number of N reflectors

result in $N+1$ uncorrelated images, and minimizing the correlation in between each two of them gives C_{N+1}^2 equations. Therefore, the number of unknowns with N reflectors is

$$N_{unknown} = 4 + 3(N - 1) = 3N + 1, \quad (2.7.3)$$

and the number of equations is

$$N_{eq} = 3 + C_{N+1}^2 = 3 + \frac{(N + 1)N}{2}. \quad (2.7.4)$$

For the equation set to be solvable, $N_{unknown} \leq N_{eq}$, N is 1 or $N \geq 4$ (Fig. 2.9), though the exact approach of solving equations needs further study.

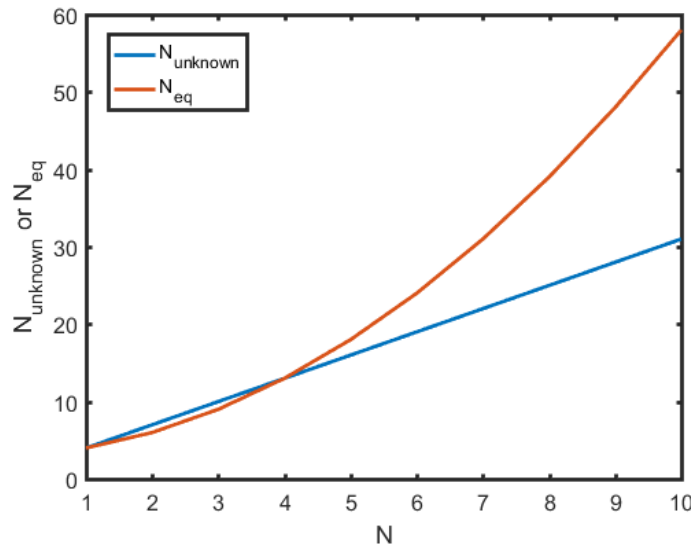


Fig. 2.9. Number of unknowns and number of equations as functions of the number of reflectors.

In practice, however, scenes with more than three reflectors are rare. When $N = 2$, as discussed above, $N_{unknown} = 7$ and $N_{eq} = 6$. If the relative location of the two reflectors is known or can be approximated, for example, the two reflectors are windows that are on the opposite sides of a

building, or one reflector is the floor while the other one is a glass door, an additional equation exists that relates $\phi_{1,2}$ and $\theta_{1,2}$, which makes the equation set solvable. When $N = 3$, $N_{unknown} = 10$ and $N_{eq} = 9$, the same additional equation exists as in the $N = 2$ case if the same assumption applies.

2.8 Discussion and Conclusions

The accuracy of image separation is affected primarily by the polarization of the light reflected from the original objects, the accuracy of the refractive index (medium) and the incident angle estimates, and the BRDF of the transparent or semi-glossy reflector, i.e. strength of the UDR component due to diffuse surface scattering. The assumption that the light from the two objects is unpolarized does not hold under all circumstances, for example, when the object surface is optically smooth, which gives rise to strong SR, i.e. glass and polished ceramics, or when the light source itself is polarized, i.e. computer screens. Nevertheless, our technique can be generalized to arbitrary polarization, if we can independently estimate the polarization of the light coming from the objects.

An inaccurate refractive index estimate can lead to inaccuracy in $R_{s,p}(\phi)$ and subsequently to artifacts (residuals and shifts in color) in the separated images. However, for materials commonly-used in daily life, indices range from $n = 1.3$ [32] (precipitated calcium carbonate, PCC) to $n = 1.79$ [36] (SF11 glass), this inaccuracy does not affect the separated object T image significantly, and it has no effect when $\phi = \phi_B$, the Brewster angle. In addition, minimization of the same metric by treating the value of the refractive index as an optimization variable may further improve the quality of the object R image. Meanwhile, inaccuracies in incident angle can

also lead to artifacts in the separated images. The diattenuation term $D^{Tr}(\phi)$ is a monotonically decreasing function of the incident angle. Therefore, when recovering the object R image, either more intensity is removed if the incident angle is underestimated or less intensity is removed if the incident angle is overestimated. This conclusion applies to object T image separation, when both the estimated incident angle and the actual incident angle are below ϕ_B , while more (less) intensity that is removed corresponds to an overestimated (underestimated) incident angle when both the estimated and the actual incident angles are above ϕ_B .

In conclusion, the separation technique in this chapter that uses polarimetric imaging and the edge overlap metric function is robust and can be applied in real-time in both indoor and outdoor environments. Objects that are not in the FoV can be imaged and measured in visible, near infrared and long wave infrared spectrum. The ideal choice of the spectrum is determined by the properties of the reflecting surface, and the ideal wavelength range corresponds to where the SNR of light received from the reflector is the highest.

Chapter 3. Polarization-based image separation with polarized objects

3.1 Polarized sources

The image separation method in the last chapter applies to unpolarized incident light on the reflector. Meanwhile, polarized light sources are becoming more and more popular due to the increasing usage of liquid crystal displays (LCDs). As displays are designed to convey information efficiently to human, acquiring such information from outside the FoV may be of more interest than acquiring the information of unpolarized objects, and the leakage of information from such sources can cause more serious information security issues.

The schematic of the optical measurement process is shown in Fig. 3.1. Similar to the physical processes with unpolarized sources described in the last chapter, an imaging polarimeter is used to capture the reflected or scattered light from the reflector. Still, the interaction of the light with the reflector includes specular reflection, specular transmission, surface scattering and volume scattering. In addition, ambient light, e.g. light from an overhead lamp, generally acts as unwanted background or noise in the separation and is typically unpolarized and uniform in terms of spatial/angular distribution. In the discussion of the separation methods below, we refer to all photon contributions to the captured image that do not result from specular reflection as the transmission component, and we do not discern further between the various transmission components. A robust separation method should provide good separation results even when these components are not modeled in detail, for in most cases, little is known about them.

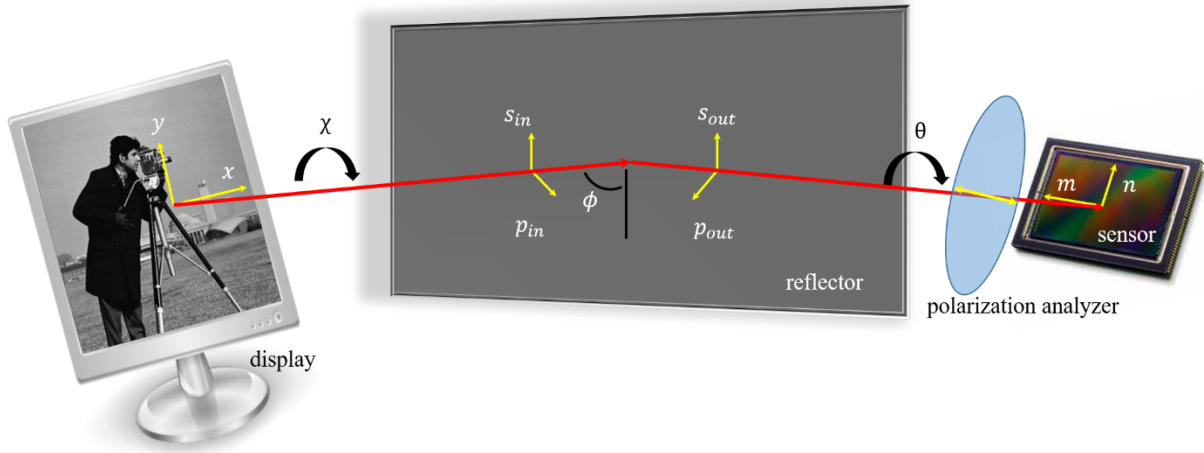


Fig. 3.1. A schematic of the scene is shown. Light emitted from a display device (image of a camera man) propagates to the reflector (gray) at an incident angle of ϕ , is reflected by the reflector, passes through the polarization analyzer (blue), and is detected by an imaging sensor. The imaging lens is not shown. Local coordinates of the display device in x, y are rotated by an angle of χ into the incident local coordinates s_{in}, p_{in} on the reflector, and the exit local coordinates s_{out}, p_{out} on the reflector are rotated by an angle of θ into the local coordinates m, n of the sensor. The horizontal direction of the polarization analyzer (in yellow) aligns with m . Modified from [22].

The LCD screens of many electronic devices emit predominantly linearly polarized light, while some others, such as the iPhone screens, emit elliptically polarized light and are designed to be visible through polarized sunglasses when the screen is rotated. Linearly polarized sources can be represented by $\mathbf{S}^{src} = S_0^{src}(1, -1, 0, 0)^T$. The source is assumed to be initially polarized along the vertical direction, as most LCDs are. Other displays, such as the iPhone screens, can be approximately described by a Stokes vector with a circular polarization component, $\mathbf{S}^{src} =$

$S_0^{src}(1, s_1, 0, \sqrt{1 - s_1^2})^T$, where s_1 is the projection of \mathbf{S}^{src} along the $0^\circ/90^\circ$ direction on the Poincarè sphere. The validity of this approximation can be shown as follows.

The iPhone screen is roughly right-handed circularly polarized at a single wavelength, the designed wavelength $\lambda_0 \approx 550$ nm. The screen can be modeled as a quarter-wave plate (QWP) placed on top of a linearly polarized source. The phase difference between the fast and slow axes of the QWP is $OPD_{QWP} = \Delta n \cdot d_{QWP}$, where Δn is the difference of refractive indices between the two axes, and d_{QWP} is the physical thickness of the QWP. For a QWP operating at λ_0 , $OPD_{QWP} = (m + 1/4)\lambda_0$ ($m \in Z$). From Jones calculus, the electric field of the light emitted from the screen, \mathbf{E}^{src} , is an integral of the Jones vector under each wavelength

$$\begin{aligned} \mathbf{E}^{src} &= \int_{\lambda_1}^{\lambda_2} A(\lambda) e^{-i\omega t} \cdot \mathbf{R}_{2D}(45^\circ) \cdot \begin{bmatrix} e^{-i\frac{\pi \cdot OPD_{QWP}}{\lambda}} & 0 \\ 0 & e^{i\frac{\pi \cdot OPD_{QWP}}{\lambda}} \end{bmatrix} \cdot \mathbf{R}_{2D}(-45^\circ) \cdot \begin{pmatrix} 1 \\ 0 \end{pmatrix} d\lambda \\ &= \int_{\lambda_1}^{\lambda_2} A(\lambda) e^{-i\omega t} \cdot \begin{bmatrix} \cos\left(\frac{\pi \cdot OPD_{QWP}}{\lambda}\right) \\ -i \sin\left(\frac{\pi \cdot OPD_{QWP}}{\lambda}\right) \end{bmatrix} d\lambda, \end{aligned} \quad (3.1.1)$$

where $\lambda_{1,2}$ are limits of the integral over wavelength, $A(\lambda)$ is the spectrum-dependent field amplitude whose magnitude square integrates to a constant ($\int_{\lambda_1}^{\lambda_2} |A(\lambda)|^2 \cdot d\lambda = S_0^{src}$), λ is the wavelength of light, $\omega = 2\pi c/\lambda n$ is the angular frequency of light, c is the speed of light in vacuum, n is the refractive index at λ , and $\mathbf{R}_{2D}(\pm 45^\circ)$ are the 2-dimensional rotation Jones matrices at angle $\pm 45^\circ$ along the z -axis (propagation direction). Without loss of generality, the linearly polarized source is also assumed to emit vertically polarized light and is thus represented by the Jones vector $(1, 0)^T$. Clearly, for applications at the designed wavelength, $A(\lambda) =$

$\sqrt{S_0^{src}} \delta(\lambda - \lambda_0)$ and \mathbf{E}^{src} evaluates as $(1, -i)^T$ to within a constant phase factor, which represents a right-handed circular polarization state. For numerical calculation of the integral, we focus on the visible spectrum ($\lambda_1 = 400nm$, $\lambda_2 = 700nm$). The change of n with the wavelength, i.e. dispersion, is assumed to be small relative to the absolute change of λ .

The integral of interest cannot be evaluated directly as it assumes that the integrand at different wavelengths add up coherently (without any phase difference), while LCDs emit incoherent light and the integrand at different wavelength add up with a random phase difference. For a more intuitive result, the Jones vector being integrated is converted first into its corresponding Stokes vector and then integrated. For a general Jones vector $E_{x,y}$ defined in the xy plane, the relationship between the Stokes vector and the Jones vector is

$$\mathbf{S} = \begin{bmatrix} |E_x|^2 + |E_y|^2 \\ |E_x|^2 - |E_y|^2 \\ 2\text{Re}(E_x E_y^*) \\ -2\text{Im}(E_x E_y^*) \end{bmatrix}, \quad (3.1.2)$$

such that the Stokes vector corresponding to \mathbf{E}^{src} becomes

$$\mathbf{S}^{src} = \begin{bmatrix} S_0^{src} \\ \int_{400nm}^{700nm} |A(\lambda)|^2 \cos\left(\frac{\pi\lambda_0}{2\lambda}\right) d\lambda \\ 0 \\ \int_{400nm}^{700nm} |A(\lambda)|^2 \sin\left(\frac{\pi\lambda_0}{2\lambda}\right) d\lambda \end{bmatrix}, \quad (3.1.3)$$

where we have applied the property of $A(\lambda)$ and have expanded OPD_{QWP} in terms of λ_0 . We therefore define the second element in the Stokes vector as $S_0^{src} s_1$, and the iPhone screen can be

approximated as an elliptically polarized source described by $S_0^{src}(1, s_1, 0, \sqrt{1 - s_1^2})^T$ according to the normalization property of the Stokes vector: $\sum_{i=1,2,3} S_i^2/S_0^2 = 1$. Deviation from the approximation becomes noticeable for wavelengths far from λ_0 . The degree of circular polarization, $DoCP = S_3/S_0$, is 1 if the light is right-handed-circularly polarized. When the source emits only 400nm light, DoCP of the source reaches a minimum of 0.83. This deviation has been observed in our experiments.

3.2 Mueller matrices

When light from the source encounters the reflector, it undergoes various processes depending on physical properties of the reflector. Therefore, we introduce a general model for \mathbf{S}^{cam} , and then explain in detail all the processes and their corresponding derivations.

$$\mathbf{S}^{cam} = \mathbf{R}_{2D}(\theta) \cdot (\mathbf{R}(\phi) \cdot \mathbf{R}_{2D}(\chi) \cdot \mathbf{S}^{Re} + \mathbf{T}(\phi) \cdot \mathbf{S}^{Tr}), \quad (3.2.1)$$

where $\mathbf{S}^{Tr,Re}$ are the Stokes vector of the light from object T and R, $\mathbf{R}(\phi)$, $\mathbf{T}(\phi)$ are the Mueller matrices for reflection and refraction/scattering on the media (their exact forms depending on the type of media), and $\mathbf{R}_{2D}(\theta)$, $\mathbf{R}_{2D}(\chi)$ are two 4×4 2-dimensional (2D) rotation matrices in the xy plane. The light from object T is assumed to be unpolarized with Stokes vector given by $(S_0^{Tr}, 0, 0, 0)^T$, where S_0^{Tr} is the irradiance.

We consider three cases with different reflectors and sources. The first case is with an uncoated surface, such as marble tiles, and a linearly polarized source. A portion of light is reflected on the surface, while the rest transmits through the surface and is subsequently volumetrically scattered or absorbed. The ratio of reflection and refraction is determined by the Fresnel equations, while the portion of light that undergoes volume scattering depends on the

porosity and exact chemical composition of the material and can be unknown to us. We note that volume scattering is assumed to create unpolarized light [37]. Both the reflected and a portion of the scattered light are captured by the camera. Therefore, in this case, the reflection Mueller matrix is [2],

$$\mathbf{R}(\phi) = \frac{1}{2} \begin{bmatrix} R_{12s} + R_{12p} & R_{12s} - R_{12p} & 0 & 0 \\ R_{12s} - R_{12p} & R_{12s} + R_{12p} & 0 & 0 \\ 0 & 0 & -2\sqrt{R_{12s} \cdot R_{12p}} & 0 \\ 0 & 0 & 0 & -2\sqrt{R_{12s} \cdot R_{12p}} \end{bmatrix}, \quad (3.2.2)$$

where $R_{12s,12p}$ are reflectances of s, p light on a surface with the light propagating from material 1 (for air, $n_1 = 1$) to material 2 ($n_2 = n_{marble}$). The reflectances are given by the Fresnel equations [38]. The transmission matrix $\mathbf{T}(\phi)$ is

$$\mathbf{T}(\phi) = a \begin{bmatrix} 1 & 0 & 0 & 0 \\ 0 & 0 & 0 & 0 \\ 0 & 0 & 0 & 0 \\ 0 & 0 & 0 & 0 \end{bmatrix}, \quad (3.2.3)$$

where a is the portion of light being volume scattered, and $\mathbf{T}(\phi)$ represents the volume scattering process.

In the second case, we consider a coated surface, such as the surface of a wooden desk and an elliptically polarized source. The physical processes on the reflector resemble those in the uncoated surface, except that the volume scattering is now replaced by surface scattering. The surface scattering often partially depolarizes the incident light and produces partially polarized light, whose properties depends on the polarized bidirectional reflectance distribution function (pBRDF) of the surface/interface, for example at the latex-wood interface of the wooden furniture. The Mueller matrix BRDF of a general depolarizer is [39]

$$\mathbf{T}(\phi) = \begin{pmatrix} 1 & \mathbf{0}^T \\ \mathbf{P}_\Delta & \mathbf{m}_\Delta \end{pmatrix}, \quad (3.2.4)$$

where $\mathbf{0}$ is a 3×1 zero vector, \mathbf{P}_Δ is a 3×1 angle-dependent polarizance vector, and \mathbf{m}_Δ is a 3×3 angle-dependent symmetric matrix. As the pBRDF of this interface depends on both the polished condition of the substrate and how the coating is applied, $\mathbf{T}(\phi)$ can vary a lot and cannot be assumed to obey any specific distribution. For the wooden surface, the latex-wood interface is generally both a weak polarizer (due to first-surface reflections) and a strong depolarizer (due to multiple surface and subsurface reflections) at oblique incidence [37]. For simplicity, we treated the latex-wood interface used in our experiment with the pBRDF of an ideal depolarizer, since all elements in \mathbf{P}_Δ and \mathbf{m}_Δ should be small based on its properties mentioned above.

For the third case, we consider the transparent window as the reflector [21]. The Mueller matrices for transmission and reflection are the same as in the last chapter with unpolarized sources.

In the above studies, we focus on discerning photons that come from specular reflection from those from refraction/scattering, while recovering some of the geometrical information of the scene, such as the angles χ, ϕ, θ . If the reflective media is in direct line of sight, the orientation of the media and the angle θ can be determined. If the rim of the screen is visible, the orientation of a screen and the angle χ can be calculated by line detection algorithms using the Hough transform.

3.3 Mueller matrix equations for image separation with polarized objects

To solve $\mathbf{S}^{Tr,Re}$ in terms of \mathbf{S}^{cam} , we list below the three sets of equations corresponding to the three cases discussed in the last section. Both \mathbf{S}^{Tr} and \mathbf{S}^{Re} are functions of the incident angle ϕ and can be obtained separately by solving the linear equations. As the two are generally uncorrelated, the correlation between the two should ideally reach a minimum for the correct ϕ corresponding to the physical setup of the scene. Note that the reflectance and transmittance are in fact functions of ϕ , and they determine the diattenuation of the reflection/transmission Mueller matrices. In this section, we focus on deriving solvable linear equations between the captured image and the source. In general, the equations are non-linear, but we show here that the problem can be approximated by linear equations.

For the first case, we consider an uncoated surface with a linearly polarized object R.

$$\mathbf{S}^{cam} = \begin{bmatrix} a \cdot S_0^{Tr} + (A_{12} - B_{12} \cos 2\chi) S_0^{Re} \\ C_{12} \sin 2\chi \sin 2\theta S_0^{Re} + \sigma_1 \cos 2\theta \\ C_{12} \sin 2\chi \cos 2\theta S_0^{Re} - \sigma_1 \sin 2\theta \\ 0 \end{bmatrix}, \quad (3.3.1)$$

where $A_{12} = (R_{12s} + R_{12p})/2$, $B_{12} = (R_{12s} - R_{12p})/2$, $C_{12} = -\sqrt{R_{12s}R_{12p}}$, and $\sigma_1 = B_{12}S_0^{Re} - A_{12} \cos 2\chi S_0^{Re}$. There are six unknowns ($\theta, \chi, \phi, S_0^{Re}, a_{ij}, S_0^{Tr}$) and four equations; thus, the inverse problem is ill-posed. We make two assumptions for the subsequent analysis. First, we only focus on recovering a but not S_0^{Tr} . Secondly, the reflective medium is assumed to be inside the FoV, such that θ can be determined from the measured image (for example, $\theta = 180^\circ$ if the medium is the ceiling). χ is solved from θ and the line detection algorithm, and the equation becomes linear.

For the second case, we consider a coated surface with a circularly polarized object R.

$$\mathbf{S}^{cam} = \begin{bmatrix} a \cdot S_0^{Tr} + (A_{12} + B_{12}s_1 \cos 2\chi)S_0^{Re} \\ -C_{12}s_1 \sin 2\chi \sin 2\theta S_0^{Re} + \sigma_1 \cos 2\theta \\ -C_{12} \sin 2\chi \cos 2\theta S_0^{Re} - \sigma_1 \sin 2\theta \\ C_{12}S_0^{Re} \end{bmatrix}, \quad (3.3.2)$$

where $\sigma_1 = B_{12}S_0^{Tr} + A_{12}s_1 \cos(2\chi)S_0^{Tr}$. Note that A_{12}, B_{12}, C_{12} have the same definitions as in the first case, but the $R_{12s,12p}$ in them are replaced by $R_{s,p}^w$ calculated from the coating's refractive index ($n_2 = n_{coat}$). Compared with the first case, there is an additional unknown, s_1 , and the number of equations is the same. Therefore, for the equations to be linear and solvable, aside from the two assumptions made in the first case, we also approximate s_1 by its value when $A(\lambda) = \sqrt{S_0}\delta(\lambda - \lambda_{R,G,B})$. $\lambda_{R,G,B} = 460, 530, 610 \text{ nm}$ correspond to the three wavelengths of peak quantum efficiency for a typical complementary metal-oxide-semiconductor (CMOS) sensor with Bayer filters [40]. Thus, we assume $s_1 = 0.1539, -0.0592, -0.3025$ for the red, green, and blue pixels, respectively. Errors from the approximation of s_1 have been observed in the experiments.

For the third case, we consider a transparent window [21] with a linearly polarized object R,

$$\mathbf{S}^{cam} = \begin{bmatrix} (A_{t,12}^2 + B_{t,12}^2)S_0^{Tr} + (\sigma_2 - \sigma_1 \cos 2\chi)S_0^{Re} \\ 2A_{t,12}B_{t,12} \cos 2\theta S_0^{Tr} + \{(\sigma_1 - \sigma_2 \cos 2\chi) \cos 2\theta + (C_{t,12}^2 + 1)C_{12} \sin 2\chi \sin 2\theta\}S_0^{Re} \\ -2A_{t,12}B_{t,12} \sin 2\theta S_0^{Tr} - \{(\sigma_1 - \sigma_2 \cos 2\chi) \sin 2\theta + (C_{t,12}^2 + 1)C_{12} \sin 2\chi \cos 2\theta\}S_0^{Re} \\ 0 \end{bmatrix}, \quad (3.3.3)$$

where $\sigma_1 = B_{12} + A_{t,12}(A_{12}B_{t,12} + B_{12}A_{t,12}) + B_{t,12}(A_{12}A_{t,12} + B_{12}B_{t,12})$, $\sigma_2 = A_{12} + A_{t,12}(A_{12}A_{t,12} + B_{12}B_{t,12}) + B_{t,12}(A_{12}B_{t,12} + B_{12}A_{t,12})$, $A_{t,12} = (T_{12s} + T_{12p})/2$, $B_{t,12} = (T_{12s} - T_{12p})/2$, and $C_{t,12} = \sqrt{T_{12s}T_{12p}}$. A_{12}, B_{12}, C_{12} and $A_{t,12}, B_{t,12}, C_{t,12}$ are calculated with

the window's refractive index ($n_2 = n_{window}$). There are five unknowns ($\theta, \chi, \phi, S_0^{Re}, S_0^{Tr}$) and four equations. Here we assume that θ is known. The equations are then solvable and linear.

3.4 Collection of separated images

Static images were acquired using a Sony DSC-RX10M3 camera with a ZEISS Vario-Sonnar T* 2.4-4/8.8-220 lens. Polarizing filters were attached in front of the camera lens and rotated manually to achieve different polarization modulation of the incoming light. The linear polarizer was a HOYA 72 mm linear polarizing filter, which is fixed in front of the camera and can be manually rotated for different polarization modulation. The corresponding orientations of the polarizer are 0° , 45° , 90° , and 135° with respect to its horizontal direction. The polarization properties of the filter were characterized beforehand with an Axometrics AxoScan polarimeter, and the Stokes images of the scene were computed with the conventional data reduction method [19, 20]. Note that although measuring the s_3 component in the iPhone case helps in solving the equations, most commercial circular polarizers are not achromatic, so either an additional narrow-band spectral filter at 550 nm should be used during all polarimetric measurements, or two achromatic circular polarizers should be used instead, which are typically more expensive. Therefore, we only measure the linear components in all the experiments.

The LCD screen, acting as a linearly polarized source, was a Dell AS501 monitor and the screen of a Toshiba Protège laptop. The screen that acted as a circularly polarized source was an Apple iPhone 6 cell phone. Screen resolutions were 1280×800 for both linearly polarized sources, and 750×1334 for the circularly polarized source. For all experiments, ambient light was provided by the same fluorescent light tube with the same brightness overhead. The

refractive indices of marble, glass, and latex coating are assumed to be 1.65, 1.52, and 1.4 respectively.

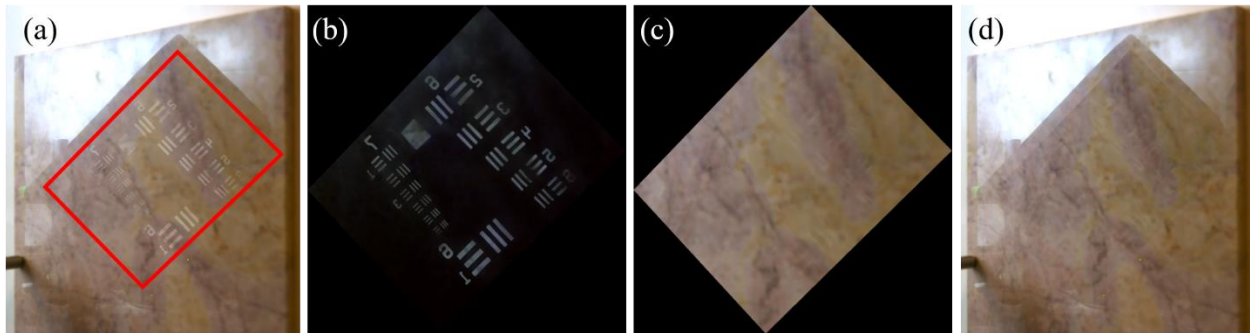


Fig. 3.2. Reflection of the monitor screen from a marble tile is shown. (a) Overlap of the image of the screen contents and the tile is denoted by a red rectangle. (b) Separated screen contents and (c) separated tile texture are shown. (d) Reflection-removed image emphasizing the continuity of irradiance over the boundary of the overlapping region is also shown. Modified from [22].

To study uncoated surfaces, a piece of marble tile was used as the reflective medium. The monitor displayed a 1951 USAF resolution target. This target was used as a general object rather than the purpose of studying the modulation transfer function (MTF) after the separation, and as such, it was not displayed at its designed resolution. For this case, θ was -90° and χ was calculated to be 134° . ϕ was measured to be 63° and recovered through EO based correlation algorithm to be 60° . The screen contents and tile texture were separated as shown in Fig. 3.2. The model of single reflection and volume scattering is found to work well, and there is no visible artifact in the separated images, especially in terms of the irradiance continuity over the boundary of the screen.

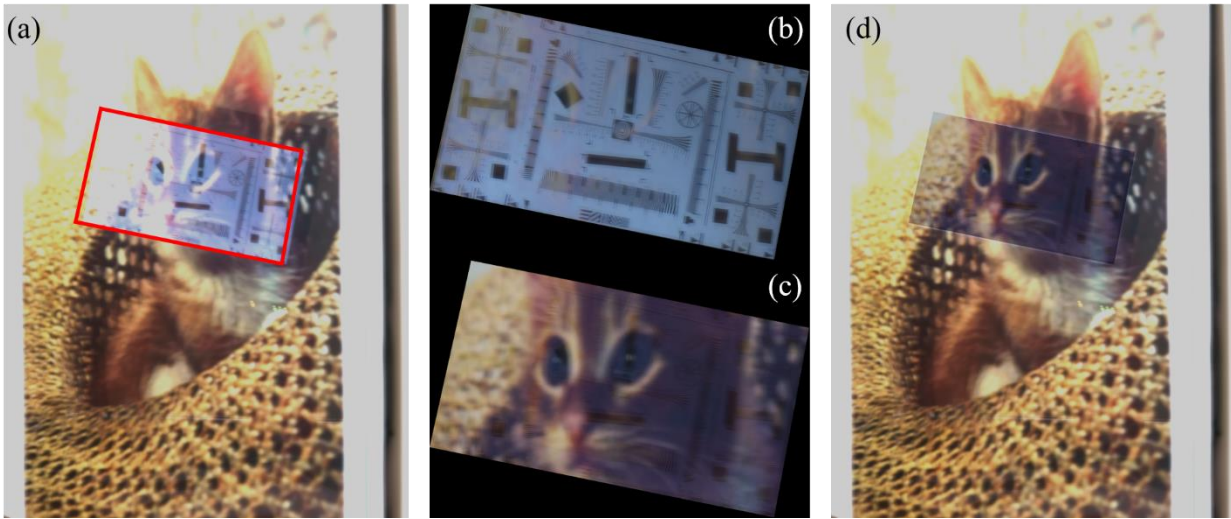


Fig. 3.3. Reflection of the laptop screen (displaying ISO 12233 test chart) from a glass-covered picture is shown. (a) Overlap of the image of the screen contents and the picture is denoted by a red rectangle. (b) Separated screen contents and (c) separated picture are shown. (d) Reflection-removed image showing discontinuity of irradiance over the boundary of the overlapping region is also shown.

For the case of transparent windows, a glass plate from a photo frame was used on top of a cat photograph. The laptop screen showed an ISO 12233 test chart, which was not displayed at its designated resolution. For this case, θ was -90° and χ was calculated to be 79° . ϕ was measured to be 47° and was recovered through algorithm to be 46° . The results are shown in Fig. 3.3. Clear separation of the test chart and the cat picture are observed. The assumption of the printer paper as a perfect depolarizer does not consider the fact that reflected light from the printer paper is also weakly polarized. This leads to a visible discontinuity in irradiance over the boundary of the screen in the separated image.

For the case of coated surfaces with a circularly polarized source, a wood sample coated with latex acted as the reflector. The cell phone screen showed a login interface with the username ‘U ARIZONA’ and the password ‘OSC’ as shown in Fig. 3.4. For this case, θ was 0° , and χ was calculated to be -1° . ϕ was measured to be 54° and was estimated by algorithm to be 55° . The screen contents and wood surface texture were separated, and the results are shown in Fig. 3.4. The separated screen image is bluish due to the approximation on the spectral response of the camera sensor. As discussed in the previous section, the s_1 component of the source’s blue channel is underestimated among the three color channels. Since $S_1^{Re} = S_0^{Re} \cdot s_1$ is recovered with relatively high accuracy, the irradiance, S_0^{Re} , of the blue channel is overestimated, resulting in the bluish tone.

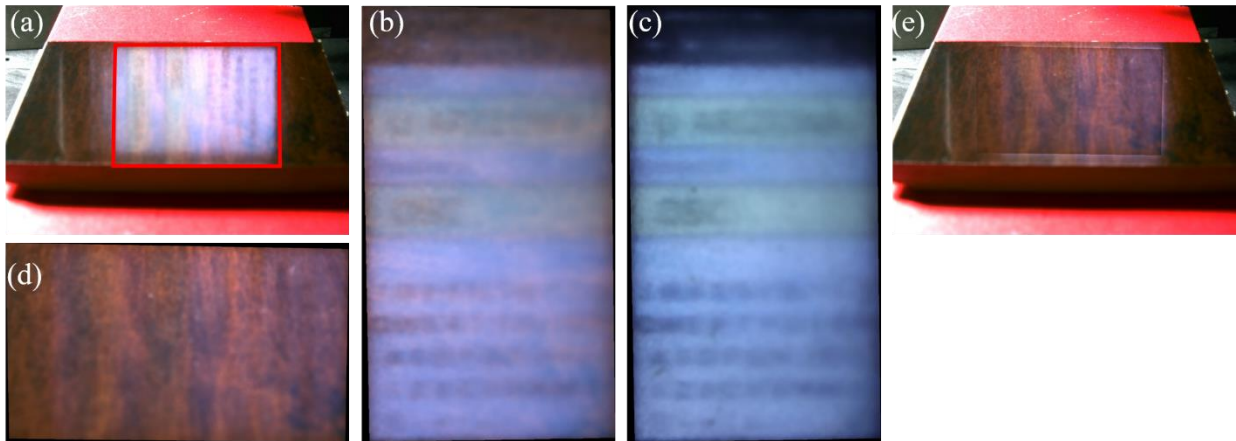


Fig. 3.4. Reflection of a cell phone screen (displaying a login screen with the username and the password) from a wood sample (overlapping region shown in red rectangle) is shown. (a) Image of the screen contents is reflected from the wood surface. (b) Overlapping image, (c) separated object R image, and (d) Separated wood surface texture image are shown. (e) Reflection-removed image shows a discontinuity of irradiance and

color over the boundary of the overlapping region. (b) and (c) are rotated for better view.

Modified from [22].

3.5 Application of filtering

In the last case with an iPhone screen, the separated contents were barely recognizable. To improve the quality of the images, the point spread function (PSF) of the reflector was measured. An 8×8 white square was displayed on the screen under the same geometry, and reflected images were taken using a mirror and a wood sample as the reflector. The PSFs of the mirror and wood sample are shown in Fig. 3.5. The standard Wiener filter using the measured PSF are applied to both the overlapping image and the separated image. Wiener filtering is a common method of image restoration for spatially-invariant system [41]. Our system can be approximated as spatially invariant because spatial variance of PSFs is mainly caused by (1) motion blur of two objects with different velocities, (2) spatially varying scattering, and (3) off-axis aberrations of the imaging system. In the experiment, the display device was stationary, and the off-axis aberrations of the camera were negligible, for the image quality is mainly limited by the pixel size of the sensor. We assumed the scattering property of the wood surface was uniform. Iterative methods that focus on spatially variant PSFs can be utilized to account for the non-uniformity of the surface's scattering property and to improve the filtering process [42].

The inputs of the Wiener filter are the optical transfer function (OTF) of the reflector, the OTF of the ideal system, both of which can be characterized beforehand, and the signal-to-noise ratio (SNR) of the measurement. The Wiener filter that includes the PSF of the camera, i.e. the ideal PSF, and the reflecting medium are given by

$$I_{filt} = IFT \left[\frac{OTF_{surf}^*}{|OTF_{surf}|^2 + SNR^{-1}} \times OTF_{mirror} \times FT(I_{unfilt}) \right], \quad (3.5.1)$$

where $I_{unfilt/filt}$ are the images before and after Wiener filtering, FT, IFT denote the Fourier transform and inverse Fourier transform, $OTF_{surf/mirror}$ are the Fourier transform of PSFs taken with the reflecting medium (wood surface) and with a flat mirror as the reflector. The SNR is defined to be the ratio of the power spectrum of the signal and the noise; its value is determined by the object and the ambient light and can be determined by estimating the specular reflected and diffuse reflection light components. Using the refractive index of latex and the estimated incident angle, SNR is estimated to be around 10. This value provides an improved image separation and is consistent with the MAD calculation using the reference image of the screen that is taken with a mirror as the reflector.

The results were then compared with the ideal image. Fidelity was measured with the mean absolute deviation (MAD), $MAD = 1/3 \sum_{r,g,b} \sum_{i,j} |\bar{I}_{i,j} - \bar{I}_{ideal;i,j}|$, where $\bar{I}_{i,j}$ and $\bar{I}_{ideal;i,j}$ are the normalized to-be-compared and ideal images with each color channel normalized to (0, 1).

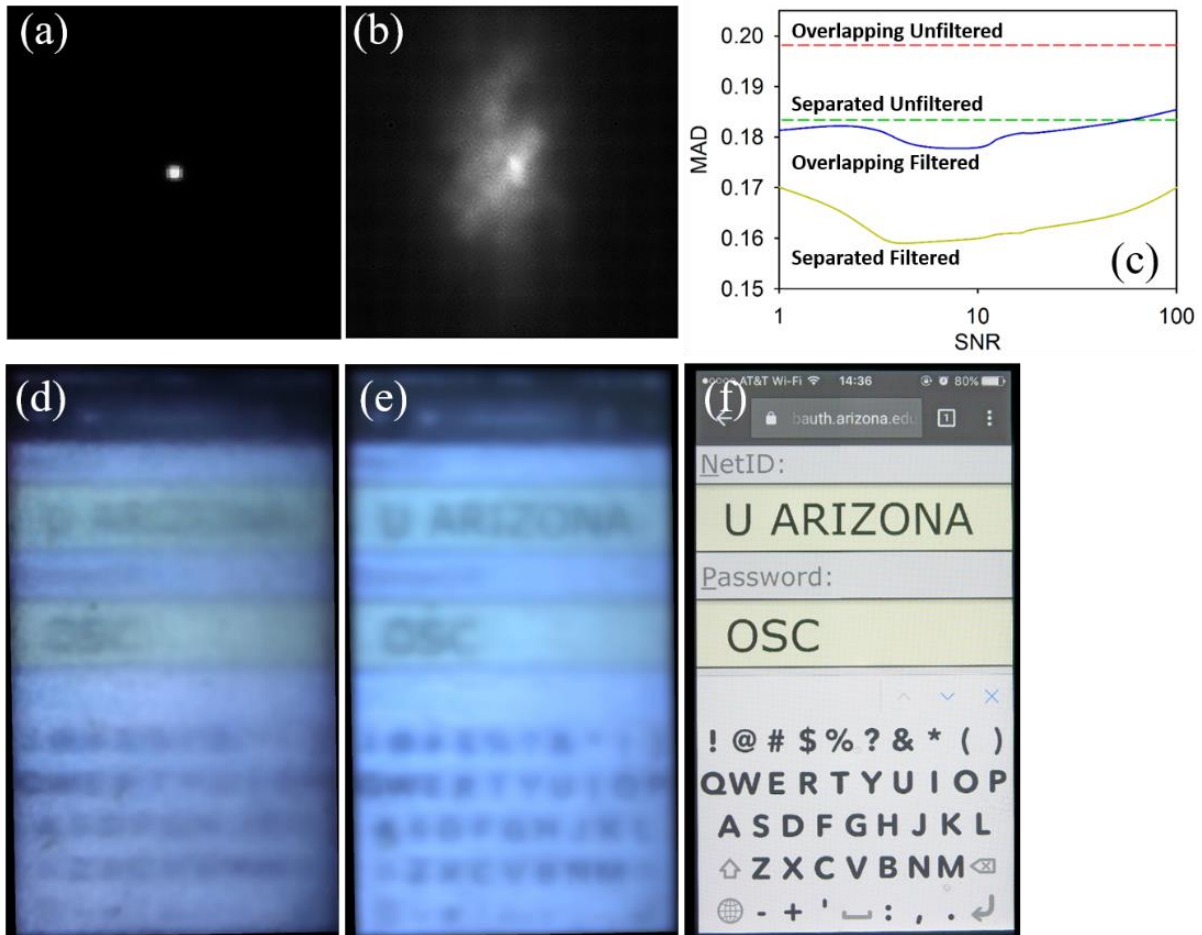


Fig. 3.5. Results with Wiener filtering. (a) PSF is measured with a mirror as the reflection surface. (b) PSF is measured with the wood surface as the reflection surface. (c) MAD plot is shown comparing the overlapping/separated images before and after Wiener filtering with the mirror-reflected image. (d) Separated image before filtering, (e) separated image after filtering, and (f) mirror-reflected image are shown. Images (d) to (f) are rotated and flipped for a better view of the screen contents. Modified from [22].

As shown in Fig. 3.5, the lowest-MAD separated filtered image has an MAD below 0.16 at an SNR of ~ 5 , and the separated filtered image quality has improved significantly with better visibility after application of the Wiener filter, though the noise induced by scattering is not fully

eliminated and the recovered image remains blurry. Note that the original image displayed on the screen is mainly in black and white. The color shift of the recovered images is caused by the assumption on the spectral response of the color filter in the DSLR camera's sensor and on the assumption of the circular polarization state of the display device.

Chapter 4. Total internal reflection in Nature

4.1 Background

The light field function [43] characterizes the radiant flux and polarization state of light along one direction at a specific spatial and temporal location. While radiant flux is the light field's measure of energy, polarization state measures the entropy of the light field [44],

$$H = - \sum_{i=1}^N P_i \log_N P_i, \quad (4.1.1)$$

where N is chosen so that $0 \leq H \leq 1$ and

$$P_i = \frac{\lambda_i}{\sum_j \lambda_j}, \quad (4.1.2)$$

where λ_i are the eigenvalues of the system coherency matrix, \mathbf{T} . One way to calculate the coherency matrix is related to the Mueller matrix of the system [44], where

$$\mathbf{T} = \begin{bmatrix} A_0 + A & C - iD & H + iG & I - iJ \\ C + iD & B_0 + B & E + iF & K - iL \\ H - iG & E - iF & B_0 - B & M - iN \\ I + iJ & K + iL & M + iN & A_0 - A \end{bmatrix} \quad (4.1.3)$$

and

$$\mathbf{M} = \begin{bmatrix} A_0 + B_0 & C + N & H + L & I + F \\ C - N & A + B & E + J & K + G \\ H - L & E - J & A - B & M + D \\ I - F & K - G & M - D & A_0 - B_0 \end{bmatrix}. \quad (4.1.4)$$

For the light field, the entropy is preserved in a physical process that has no net polarization effect and increases (or decreases) when the net effect of the optical system is depolarizing (or

polarizing). For example, diffuse scattering increases the light field's entropy and depolarizes the light, while specular reflection preserves the light field's entropy and DoP.

The polarization state of the light field generally has unpolarized, linearly polarized (LP) and circularly polarized (CP) components. Compared with the first two components, the circularly polarized component is robust against depolarization per polarization memory, introduces less entropy into the light field, and preserves the most information in scattering processes [44]. However, circular polarization, and more generally, elliptical polarization (EP) state of light are rarely seen in nature. CP light is observed in radiation from distant celestial bodies [45, 46], reflection from chiral materials [2, 47] as well as animal skin and exoskeletons [48-50], bioluminescence [51, 52], and total internal reflection (TIR) [53] of polarized light. Current studies of CP and EP in nature focus more on their biology-related origins and less on TIR, which is common in Nature [53].

TIR occurs when light is incident on an interface from a high to a low refractive index material (n_2 to n_1) at an angle greater than the critical angle (θ_c). The critical angle is

$$\theta_c = \sin^{-1} \frac{n_1}{n_2}, \quad (4.1.5)$$

and the Mueller matrix for TIR is [54]

$$\mathbf{M}_{TIR} = \begin{bmatrix} 1 & 0 & 0 & 0 \\ 0 & 1 & 0 & 0 \\ 0 & 0 & -\cos \delta & \sin \delta \\ 0 & 0 & -\sin \delta & -\cos \delta \end{bmatrix}, \quad (4.1.6)$$

where $\delta = \delta_s - \delta_p$ is the retardance induced by TIR, $\delta_s = 2 \tan^{-1} \left(\frac{\sqrt{n^2 \sin^2 \theta_i - 1}}{n \cos \theta_i} \right)$, $\delta_p = 2 \tan^{-1} \left(\frac{n \sqrt{n^2 \sin^2 \theta_i - 1}}{\cos \theta_i} \right)$, θ_i is the incident angle on the interface, and $n = n_2/n_1$. Note that the coordinate transformation due to reflection is also incorporated into \mathbf{M}_{TIR} .

4.2 Total internal reflection in inferior mirages

Inferior mirages are caused by the refractive index's gradient of air. Light propagates obliquely from the low-index side to the high-index side in air and is bent towards the low-index side during the propagation. At some point, the angle between the light's propagation direction and the refractive index's gradient is small so that the TIR condition is reached and the light is reflected. The gradient in air is typically caused by the inhomogenous heating of the air, which is often found above the ground at a hot summer day.

A model of multiple-layered dielectric plates can describe the inferior mirage (Fig. 4.1). The stack consists of a total number of N dielectric plates of a total thickness of t . The refractive index of the first layer is n_2 and that of the last layer is n_1 , which are both function of the temperature. The refractive index's gradient, Δn , is uniform in the stack,

$$\Delta n = \frac{n_2 - n_1}{N - 1}. \quad (4.2.1)$$

The thickness of each layer is $\Delta t = t/N$.

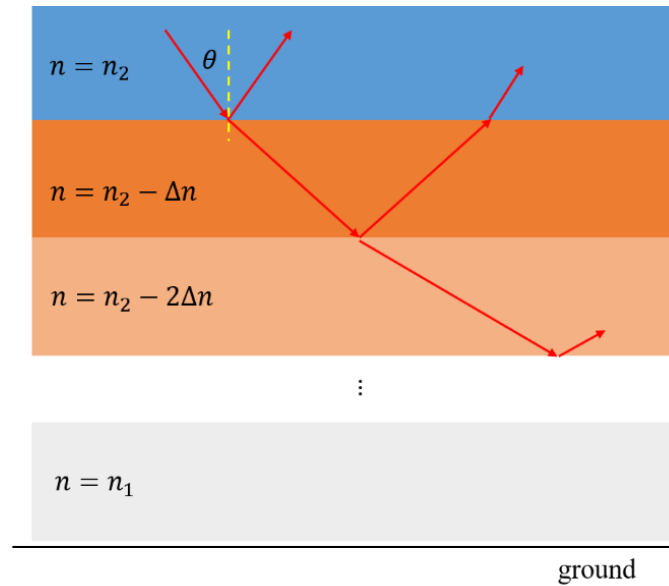


Fig. 4.1. Schematic of the multiple-layered dielectric plate model. θ is the incident angle on the first interface.

The multiple interfaces inside the stack generate multiple reflections. Since the illumination of the scene is usually sun light and there is typically fluctuation in the air's index profile, the phases of the reflections are disturbed, and the reflections are incoherent with each other. Therefore, Stokes formalism instead of the Jones formalism should be used.

When the stack is thick, the multiple reflections spread out on the detector and results in a line-shaped point-spread-function on the scale of t . A clear mirage thus requires a thin stack of air, which occurs when the temperature of the ground is high, and the light is thus bent after propagating a relatively short distance. Meanwhile, when the stack is thin, all reflections add up incoherently.

Let the incident light's Stokes vector be denoted by \mathbf{S} . To derive the resulting Stokes vector after TIR with N layers, we start with four layers as it has three interfaces. The indices of the four layers are $n_2, n_2 - \Delta n, n_2 - 2\Delta n, n_1$. The Stokes vector of the reflected light is

$$\begin{aligned}\mathbf{S}' &= \mathbf{R} \cdot \mathbf{S} + \mathbf{T} \cdot \mathbf{R}^w \cdot \mathbf{T} \cdot \mathbf{S} + \mathbf{T} \cdot \mathbf{R}^w \cdot \mathbf{R} \cdot \mathbf{R}^w \cdot \mathbf{T} \cdot \mathbf{S} + \dots \\ &= (\mathbf{R} - \mathbf{R}^w \cdot \mathbf{R}^2 + \mathbf{R}^w \cdot \mathbf{T}^2)(\mathbf{1} - \mathbf{R}^w \mathbf{R})^{-1} \cdot \mathbf{S},\end{aligned}\quad (4.2.2)$$

where \mathbf{R}, \mathbf{T} are the reflection/transmission Mueller matrix of the interface between n_2 and $n_2 - \Delta n$, and \mathbf{R}^w is the reflection Mueller matrix for the transparent window $n_2 - \Delta n, n_2 - 2\Delta n, n_1$. Equivalently, the Mueller matrix is

$$\mathbf{R}_{N=4} = (\mathbf{R} - \mathbf{R}^w \cdot \mathbf{R}^2 + \mathbf{R}^w \cdot \mathbf{T}^2)(\mathbf{1} - \mathbf{R}^w \mathbf{R})^{-1}. \quad (4.2.3)$$

The reflection Mueller matrix of N layers can be computed with an iterative process

$$\mathbf{R}_N = (\mathbf{R} - \mathbf{R}_{N-1} \cdot \mathbf{R}^2 + \mathbf{R}_{N-1} \cdot \mathbf{T}^2)(\mathbf{1} - \mathbf{R}_{N-1} \mathbf{R})^{-1}, \quad (4.2.4)$$

or deduced by tracing all the reflected rays and adding all the Stokes vectors of multiple reflections.

TIR introduces retardance into the incident light. Figure 4.2 shows the retardance in the Mueller matrix under various N and compares them with the retardance introduced by the interface of n_1 and n_2 with the same incident angle. It is seen that with an increasing N , the retardance decreases. Therefore, when the stack approaches smoothly varying gradient-index ($\Delta n \rightarrow 0$, or equivalently, $N \rightarrow \infty$), the TIR introduces no retardance into the mirage. The physical interpretation is as follows. As the incident angle on the last interface increases, the

retardance on that interface decreases; since no other interface induces retardance, the total retardance induced by the reflection of multiple-layered stack decreases.

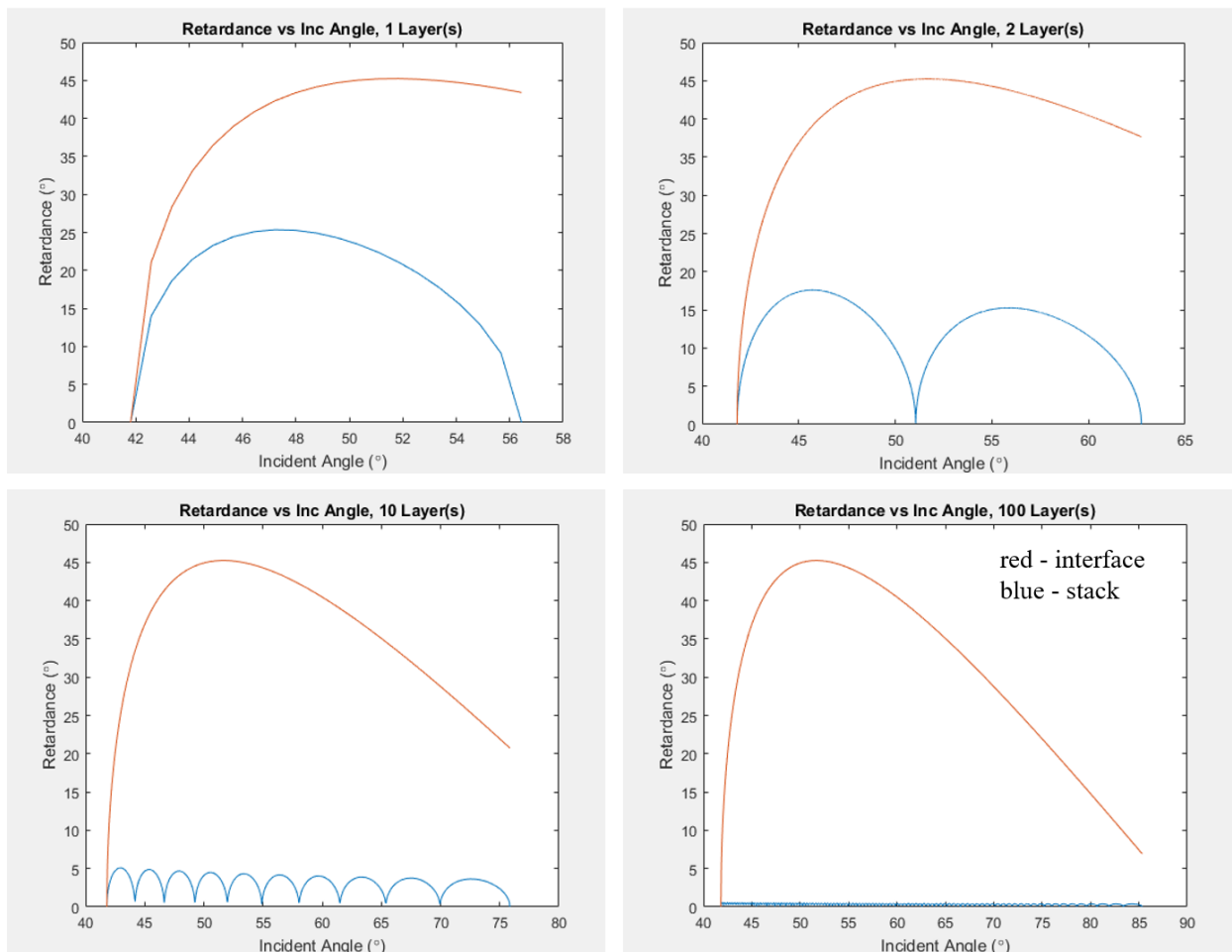


Fig. 4.2. Retardance under various N . The red curves denote the one-interface case, and the blue curves denote the multiple-layered stack case.

4.3 Other examples of TIR in Nature

TIR are also seen in rainbows, white halos and underwater scenes. Rainbows are formed by TIR of the sunlight inside the water drops that are high in the sky. Therefore, rainbows are typically observed after the rain. Depending on the number of times that light reflects inside the water

drops, the order of rainbows is defined, with order 1 the most commonly-observed rainbows and 5 the highest order that has been observed [55]. Since the sunlight that has not been scattered in the atmosphere is unpolarized, and all refractions and reflections related to the water drops happen in a plane, the rainbows are linearly polarized.

Halos are formed by reflection and/or refraction of the sunlight on ice crystals. There are two types of halos: the colored halos and the white ones. The colored halos come from the refraction of the sunlight and they show weak polarization signals, while the white halos come from the reflection of the sunlight (including TIR). However, like in the rainbow case, the sunlight that has not been scattered is unpolarized. Therefore, when the light of the halo comes mainly from TIR, its polarization signal is weak if not zero.

In the case of underwater scenes, there are generally two sources of polarized incident light in TIR: the illumination source of the scene, which is typically the sunlight that has been scattered in the atmosphere and then transmits through the air-water interface, and the reflection on the underwater objects. Light from the sky has been observed to be highly polarized with a DoLP up to 0.85 and a predicted DoLP of ~ 0.94 by single Rayleigh scattering and molecular depolarization [56, 57]. The primary mechanisms of polarized light generation in sunlight are single scattering by gas molecules and small particulates as well as multiple scatterings by clouds, aerosols, and ground surfaces. Therefore, unlike in the cases of rainbows and halos, TIR in underwater scenes can produce circularly polarized signals. We will thus study this topic in detail in the next chapters.

Chapter 5. Circular polarization under water

5.1 Distribution of circular polarization under water

The water-air interface is a unique habitat where many organisms live with specialized adaptations. The interface is also a source of TIR under water, where polarized light is seen by eyes of marine animals. The perception of CP and EP light in animal vision has been studied, and visual systems capable of detecting CP light has been observed in stomatopod crustaceans such as the Mantis shrimp [58]. The Mantis shrimp typically lives near shores, where the water is shallow (5–10 m) [59], i.e., close to the air–water interface. According to our study, we propose that CP vision can help the Mantis shrimp to better identify a predator or a prey. First, when a moving object draws close, the Mantis shrimp can tell the TIR image of the object from the object itself using the CP vision, for the light from the object contains LP component while the light from TIR contains both LP and CP components. Secondly, a benefit of CP vision comes from an inverse relationship between the albedo of the underwater object and the DoCP of its TIR image (similar to the Umov effect [60]), and thus the darker the object is under conventional imaging, the “brighter” its TIR image appears in the CP vision of the Mantis shrimp. This chapter studies the distribution of CP due to TIR and then the inverse relationship between albedo and DoCP.

Figure 5.1 shows a schematic of the underwater TIR study. The beam that illuminates the scene is described by a Stokes vector $\mathbf{S} = S_0[1, \cos \psi, \sin \psi, 0]^T$, where S_0 is the irradiance of the beam, ψ is the orientation of the linearly polarized electric field, and T denotes transpose operation. For simplicity, we assume that water surfaces are illuminated by linearly polarized

beam with a DoLP of 1, while partially polarized illumination source decreases the DoP of light after TIR. In addition, we assume normal incidence of light on the water surface for simplicity, while a non-zero solar zenith angle or a wavy water surface can result in oblique incidence of light. The oblique incidence leads to a rotation of the plane of linear polarization and a non-symmetric distribution of DoCP as a function of the incident angle, and the latter case requires further study. The transmitted beam then reflects from an underwater object, undergoes TIR at the water-air interface with an incident angle of θ , and becomes elliptically or circularly polarized.

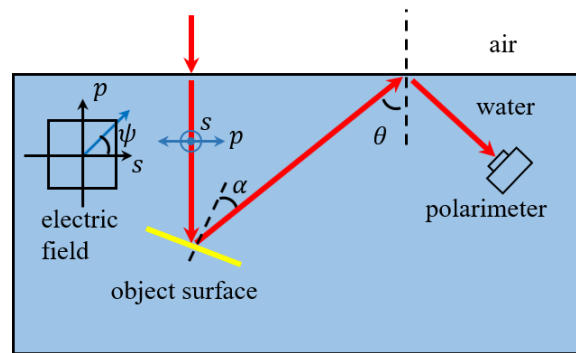


Fig. 5.1. Schematic of the scene. The incident angle on the object satisfies $\alpha = \theta/2$.

Modified from [61].

The conversion efficiency from linear polarization in the incident light to circular polarization in the TIR light, η , is defined as the ratio of the energy in the linearly polarized component in the incident light over the energy of the circularly polarized component in the TIR light. The decomposition of the Stokes vector into unpolarized, linearly polarized, and circularly polarized components gives

$$\mathbf{S} = S_0 \cdot (1 - DoLP) \cdot \begin{pmatrix} 1 \\ 0 \\ 0 \\ 0 \end{pmatrix} + S_0 \cdot DoLP \cdot \begin{pmatrix} 1 \\ \frac{s_1}{DoLP} \\ \frac{s_2}{DoLP} \\ 0 \end{pmatrix}, \quad (5.1.1)$$

and

$$\mathbf{S}' = S_0 \cdot (1 - DoLP' - DoCP) \cdot \begin{pmatrix} 1 \\ 0 \\ 0 \\ 0 \end{pmatrix} + S_0 \cdot DoLP' \cdot \begin{pmatrix} 1 \\ s_1 \\ \cos \delta \cdot s_2 \\ 0 \end{pmatrix} + S_0 \cdot DoCP \cdot \begin{pmatrix} 1 \\ 0 \\ 0 \\ 1 \end{pmatrix}, \quad (5.1.2)$$

where $DoLP'$ is the DoLP of TIR light. Therefore, the conversion efficiency is

$$\eta = \frac{S_0 \cdot DoCP}{S_0 \cdot DoLP} = \frac{|\sin \delta| \cdot |\tan 2\phi|}{\sqrt{1 + \tan^2 2\phi}}, \quad (5.1.3)$$

where $\phi = (1/2) \cdot \tan^{-1} s_2/s_1$ is the AoLP of incident light on the water-air interface. Note that ϕ is different from ψ , for the reflection on the underwater object rotates the AoLP. Since neither δ nor ϕ is a function of DoLP, the DoCP of the TIR light is proportional to the DoLP of incident light. The equation to calculate δ is introduced at the beginning of chapter 4 and is repeated here for completeness,

$$\delta = 2 \tan^{-1} \left(\frac{\sqrt{n^2 \sin^2 \theta - 1}}{n \cos \theta} \right) - 2 \tan^{-1} \left(\frac{n \sqrt{n^2 \sin^2 \theta - 1}}{\cos \theta} \right), \quad (5.1.4)$$

where $n = n_{water}/n_{air}$, n_{water} is the refractive index of water and n_{air} is the refractive index of air.

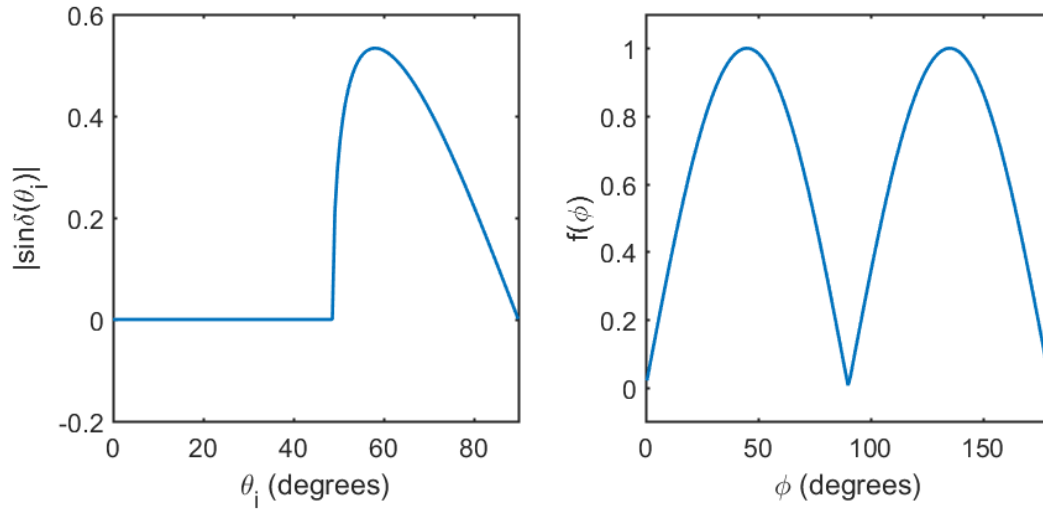


Fig. 5.2. $|\sin \delta(\theta_i)|$ and $f(\phi)$. Modified from [61].

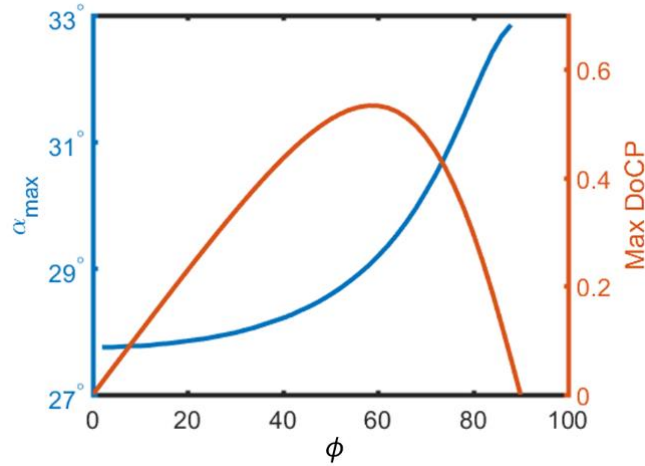


Fig. 5.3. Variation of the maximum DoCP versus ϕ (orange) and the maximum DoCP location versus ϕ (blue). Modified from [61].

Since θ and ϕ are independent of each other, the maximum of η is the product of the maximum of $|\sin \delta(\theta)|$ and the maximum of $f(\phi) = |\tan 2\phi|/\sqrt{1 + \tan^2 2\phi}$. As shown in Fig. 5.2, $f(\phi)$ has a maximum of 1 when $\phi = \pi/4$, and $|\sin \delta(\theta)|$ has a maximum of 0.53 when $\theta = 60.1^\circ$.

The maximum DoCP detected by the polarimeter and the corresponding orientation of the object surface at the maximum DoCP, α_{max} , are functions of ϕ (Fig. 5.3). The maximum occurs at α_{max} between 28° and 33° , and its peak value remains 0.53.

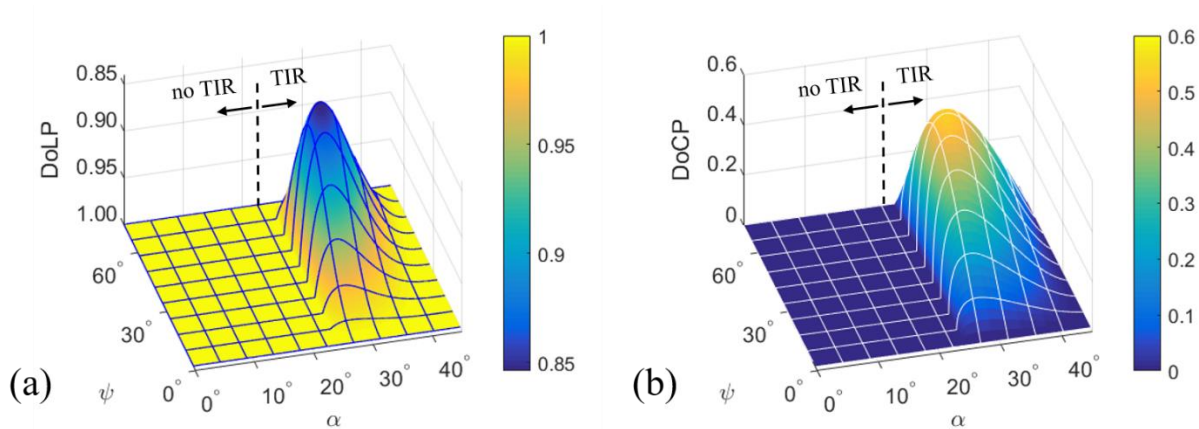


Fig. 5.4. DoLP and DoCP as functions of α and ψ . (a) Variation of DoLP versus α and ϕ .

Note that the DoLP axis has a reverse direction. (b) Variation of DoCP versus α and ϕ .

Modified from [61].

Inside Snell's window, DoLP remains 1, and no CP is detected; outside Snell's window, LP (Fig. 5.4a) is converted to EP and CP (Fig. 5.4b), with the maximum conversion peaks at around $\alpha = 30^\circ$, $\phi = 60^\circ$. Therefore, the TIR of an underwater object illuminated by polarized sky light can have a sizable component of CP or EP.

5.2 The Umov effect

The Umov effect [60, 62] states that the DoLP of scattered light from an object is inversely proportional to the object's albedo (w). The inverse relationship has its origin from unpolarized background scattering, such as subsurface scattering, that is added to the linearly polarized light

signal in specular reflection. The rigorous proof is as follows. The DoLP of scattered light from an object is[60]

$$DoLP = \frac{\Delta p}{p + \left[H\left(\frac{\mu_{0e}}{K}\right) \cdot H\left(\frac{\mu_e}{K}\right) - 1 \right]}, \quad (5.2.1)$$

where p is the volume-average single-particle phase function (VSPF) that describes the angular distribution of scattered light of a group of particles, Δp is the difference of VSPF between two orthogonal linear polarization directions (e.g. 0° and 90°), H is the Ambartsumian-Chandrasekhar H function, K is the porosity coefficient, and $\mu_{0e,e}$ are directional cosines of incident and scattering angles.

An approximated formula of the H function is[60]

$$H(x) \approx \frac{1 + 2x}{1 + 2x\sqrt{1-w}}, \quad (5.2.2)$$

where w is the volume-average single-scattering albedo. This formula approximates the H function with less than 4% error everywhere. Assuming that w is small compared to 1, the H function can be approximated by the first term in its Taylor expansion at $w = 0$, and we have

$$H(x) \approx (1 + 2x) \cdot \frac{1}{1 + 2x\left(1 - \frac{1}{2}w\right)} = \left(1 - \frac{x}{1 + 2x}w\right)^{-1} \approx 1 + \frac{x}{1 + 2x}w. \quad (5.2.3)$$

Therefore, DoLP can be approximated when w is small as

$$DoLP \approx \frac{\Delta p}{p + \left[\frac{\mu_{0e}}{K + 2\mu_{0e}} + \frac{\mu_{0e}}{K + 2\mu_{0e}} \right] w}, \quad (5.2.4)$$

where the w^2 term is ignored.

To within 4% of error, K can be approximated as[60]

$$K \approx \left(1 - 0.605 \cdot \phi^{\frac{2}{3}}\right)^{-1}, \quad (5.2.5)$$

where ϕ is the filling factor. $\phi = 0$ when the object is completely occupied by scattering particles, and $\phi = 1$ when the object is not occupied. Typically, $\phi \sim 0.2 - 0.6$, and $K \sim 1.3 - 1.8$. For example, Blackbird clay has an average ϕ of 0.25[63] and K of 1.32, and well-sorted sand (sand with similar particle sizes) has $\phi = 0.58$ [64] and $K = 1.73$. For the following calculation, we take $K = 1.5$ as an example.

When the object is diffuse, the specular reflection is a small portion of the albedo ($p \leq 0.1w$). For moderate incident and scattering angles, for example, 45° , DoLP is approximately given by

$$DoLP \approx \frac{\Delta p}{p + w} \approx \frac{\Delta p}{w}, \quad (5.2.6)$$

which is an inverse relation between the DoLP and the albedo when the signal of specular reflection is fixed. As low albedo objects and high albedo objects differ mainly in diffuse reflection instead of specular reflection, the two types of objects have similar Δp , but the high albedo objects have greater w ; hence, we have the Umov effect

$$DoLP \propto \frac{1}{w}. \quad (5.2.7)$$

In our study, the CP and EP signals detected by the polarimeter is converted from the linearly polarized scattered light through TIR, which has relatively low loss. A portion of DoLP in the

incident light is converted to the DoCP after TIR with a conversion efficiency independent of DoLP and a maximum conversion efficiency of 53%. The Umov effect leads to an inverse relationship between DoCP and the albedo of an object,

$$DoCP = \frac{C \cdot \eta(\theta, \phi)}{w} \quad (5.2.8)$$

where C is a constant related to the surface/material properties of the reflection surface (e.g. strength of surface scattering).

5.3 Collection of Stokes images

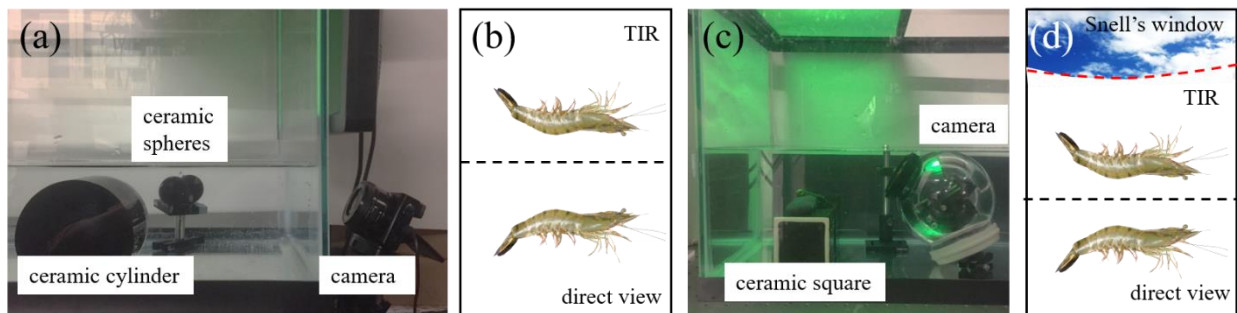


Fig. 5.5. Experimental configurations and corresponding camera views. (a) Configuration with the camera outside the tank. (b) Expected image captured by the camera with the configuration in (a). (c) Configuration with the camera enclosed in a water-proof glass globe inside the tank. (d) Expected image captured by the camera with the configuration in (c). Modified from [61].

Our calculation is demonstrated by a set of indoor imaging experiments, where a liquid crystal display (LCD) that emits linearly polarized light is used to simulate light from the sky. We consider green light with wavelength centered at 550nm, where the LCD emission is peaked. Two configurations are utilized to acquire the Stokes images using an imaging polarimeter

placed inside and outside a water tank. The corresponding camera views are illustrated in Fig. 5.5. The location of the LCD screen can be oriented to reproduce light from the sky at different times of day.

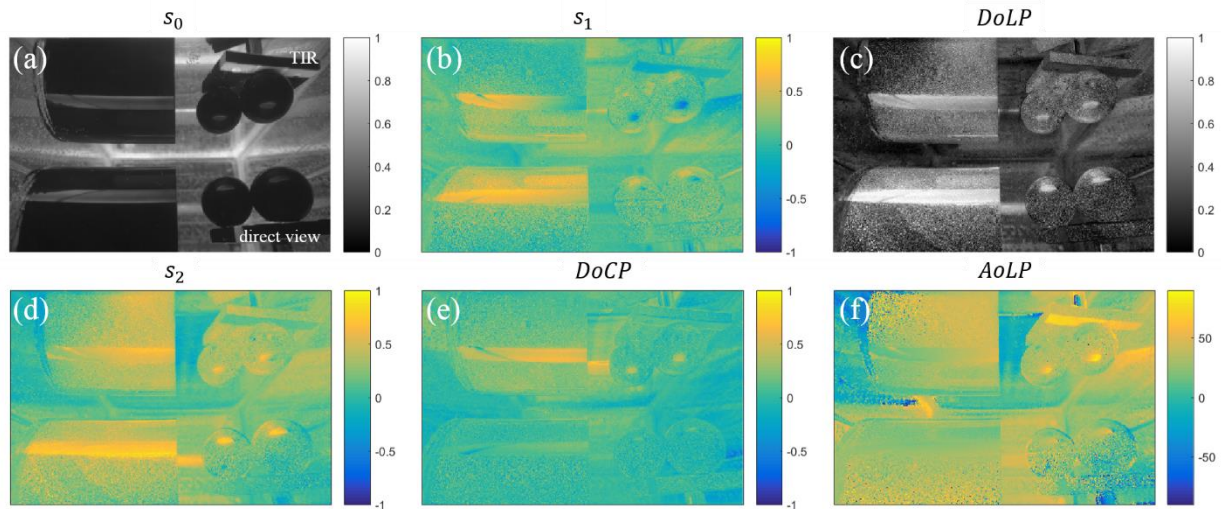


Fig. 5.6. Stokes images of a ceramic cylinder and two ceramic spheres under water.

Modified from [61].

Reflection of low-albedo or dark objects mainly consists of a specular reflection component. Figure 5.6 shows the direct and TIR views of a black ceramic cylinder and two black ceramic spheres submerged in water. In the direct view, specular reflection from the objects is linearly polarized with $DoLP \sim 1.0$. In the TIR view, the reflected image is elliptically polarized with $DoLP < 0.9$ and $DoCP > 0.5$.

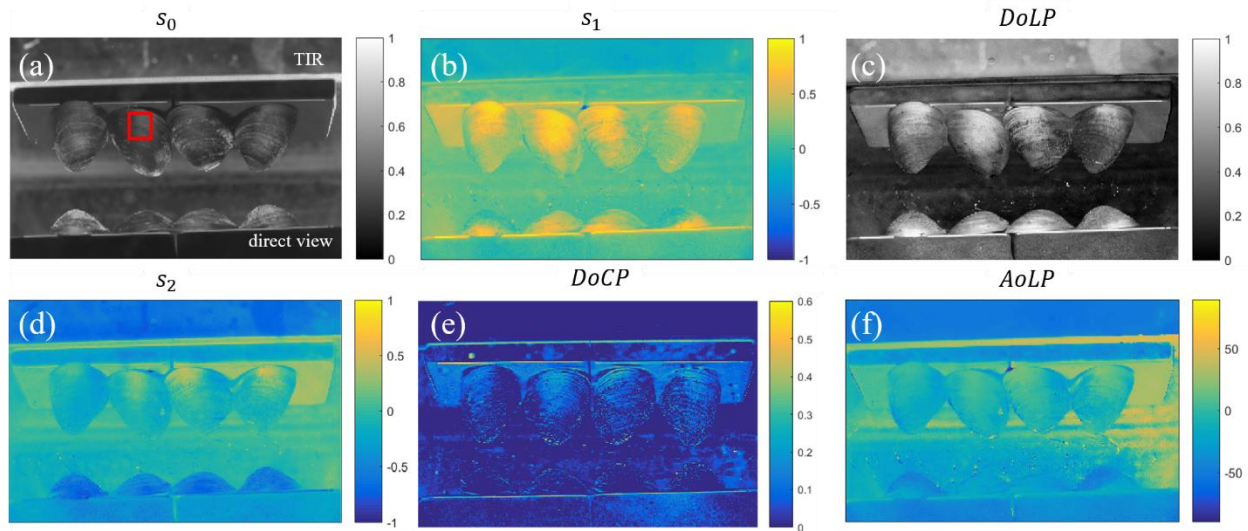


Fig. 5.7. Stokes images of four black mussels under water. Regions in red rectangles are used in the study of the Umov effect since it contains the specular reflection component. Note that the shells are curved and specular reflection does not happen all across the shells. Modified from [61].

Figure 5.7 show the direct and TIR views of black mussels in water. The rough exoskeleton of the mussel acts as a depolarizer, which causes multiple scattering of incident light. In general, both the DoLP and DoCP of the mussels are observed to be less than that of the ceramic objects. High DoLP, up to ~ 1.0 , in the direct view, and high DoCP, up to 0.5, in the TIR view can be observed.

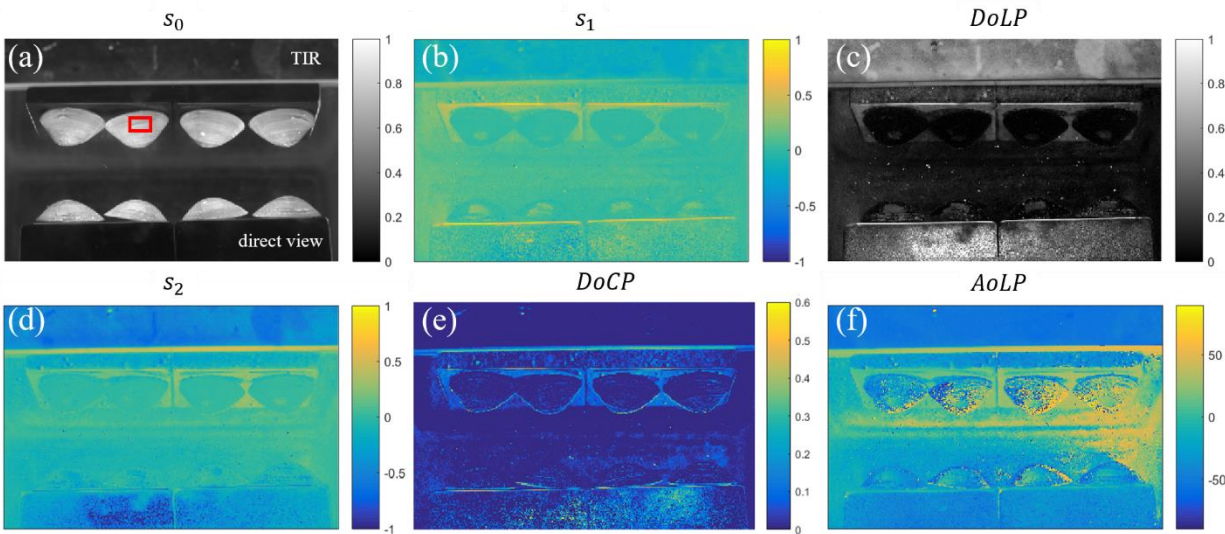


Fig. 5.8. Stokes images of four white clams underwater. Regions in red rectangles are used in the study of the Umov effect since it contains the specular reflection component. Note that the shells are curved and specular reflection does not happen all across the shells.

Figure 5.8 show the Stokes images of white clams with high-albedo under the same experimental configuration as with the black mussels. Comparison of the clams and the mussels shows the effect of albedo on the polarization state of the reflected light. An inverse relationship between DoCP and albedo is seen in the TIR view. High DoCP, up to 0.5, is observed on the black mussels, and low DoCP, up to 0.1, is observed on the white clams. The Umov effect is seen in the DoLP images. Both the direct and TIR views of the black mussels show high DoLP, up to 1.0, while those of the white clams show a low DoLP up to 0.2.

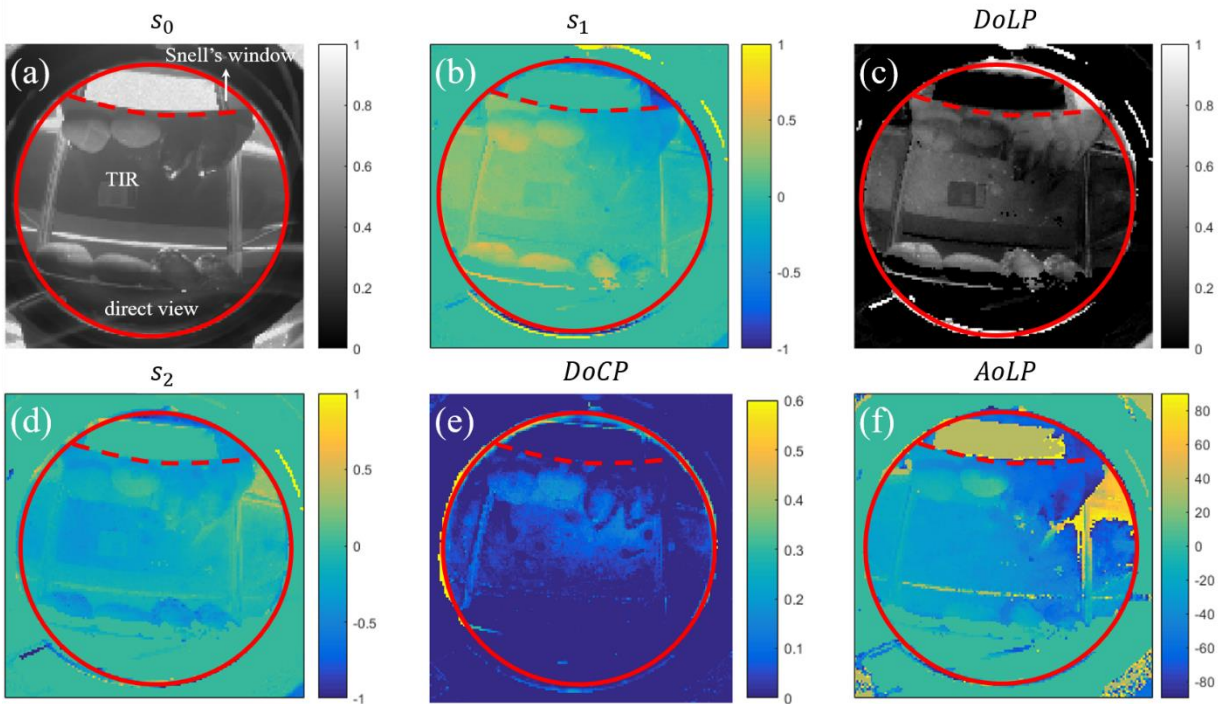


Fig. 5.9. Stokes images of two stones and two black mussels under water. In (a-f), the region of interest is inside the red solid circle, and Snell's window is highlighted with a red dashed line. Polarization measurement is noisy outside the region of interest due to its low signal.

In the camera-in-water experimental configuration, Snell's window is captured with both the direct and TIR views as shown in Fig. 5.9. The object inside Snell's window is a piece of white printer paper that scatters light and shows little polarization signal in both views. Meanwhile, high DoCP is seen in the TIR view, and the DoLP in the direct view is stronger than that in the TIR view. This demonstrates the conversion of DoLP into DoCP through TIR. The conversion efficiency depends on the incident angle of light on the water-air interface and AoLP of incident light, but not the exact value of DoLP. In general, the DoCP of the TIR light is a linear function of DoLP of the incident light.

The DoCP of objects of different albedo is shown in Fig. 5.10. The average DoCP and average albedo (S_0) of four samples underwater show an inverse relationship of $DoCP = 2.2W \cdot m^{-2}/w$, where the unit of w is $W \cdot m^{-2}$ and DoCP is dimensionless.

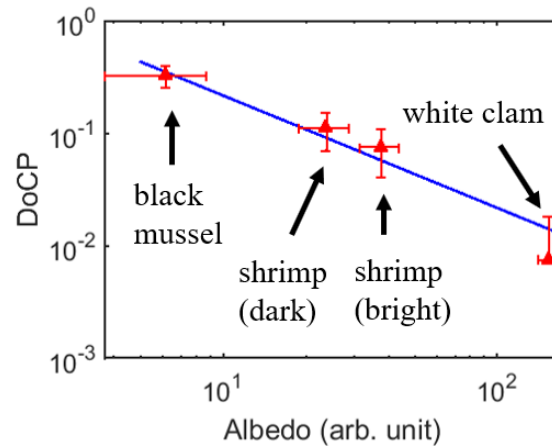


Fig. 5.10. Inverse relationship between DoCP and albedo of four samples underwater. Solid line is fitted for an inverse relation. Note that the error bars are asymmetric under log scale.

In conclusion, high CP and EP signals are observed outside Snell's window for objects under water. There is a large difference in the DoCP and DoLP between the TIR and direct views of underwater objects. For animals with CP vision, these differences can potentially be used to identify direct view and reflection of predators or prey. Under polarized illumination from the sky, the exact values of DoCP and DoLP for underwater objects depend on the albedo of the object and can be described by the Umov effect.

Chapter 6. Study of air bubbles under water

6.1 Distribution of DoCP around a bubble

When there are air bubbles under water, LP light can be converted to CP or EP light through TIR on the surface of the bubble. Considering a collimated beam of LP light shining on a bubble, the central portion of the beam refracts/reflects on the bubble while the peripheral portion undergoes TIR (Fig. 6.1), for the incident angle increases from the center of the bubble to the outward. In this way the bubble acts as an underwater CP or EP illumination source, and it is thus of interest to find the distribution of CP component around the bubble and the amount of light that is converted to circular polarization component.

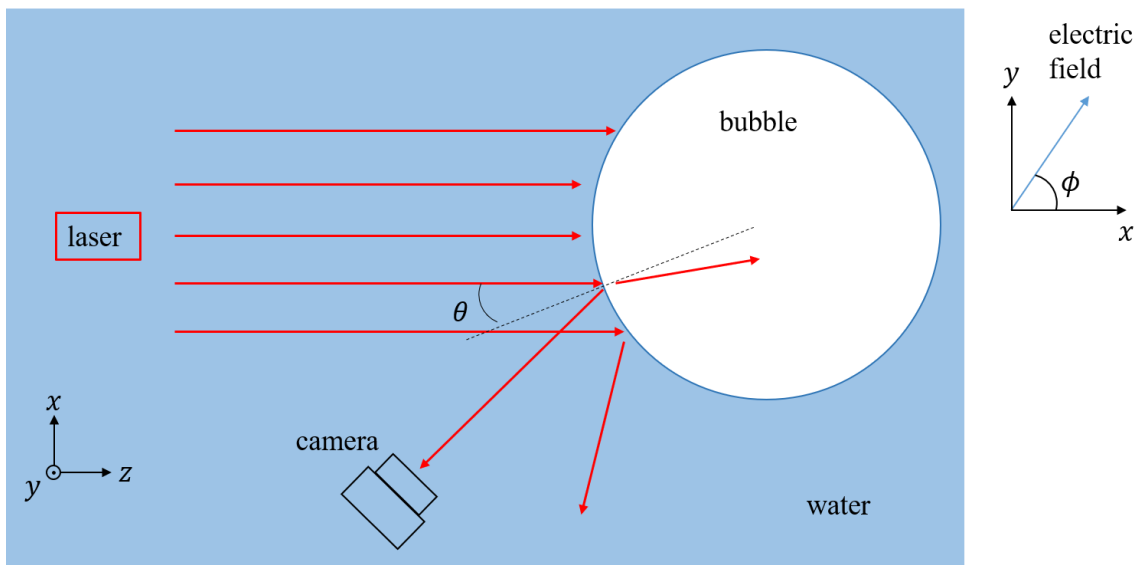


Fig. 6.1. Schematic of the refraction/reflection and TIR on an underwater air bubble under collimated laser illumination. θ is the incident angle on the bubble. The electric field of the incident light lies in the xy plane and ϕ , the AoLP, is measured from the positive x direction to the positive y direction.

As shown in Fig. 6.2, with vertically polarized incident light (polarized in the y direction, or $\text{AoLP} = 90^\circ$), the conversion efficiency (η , defined in the last chapter) in the TIR light shows a four-fold degeneracy. It comes from the fact that the conversion efficiency is proportional to $|\sin 2\phi|$, where ϕ is the AoLP of the incident light.

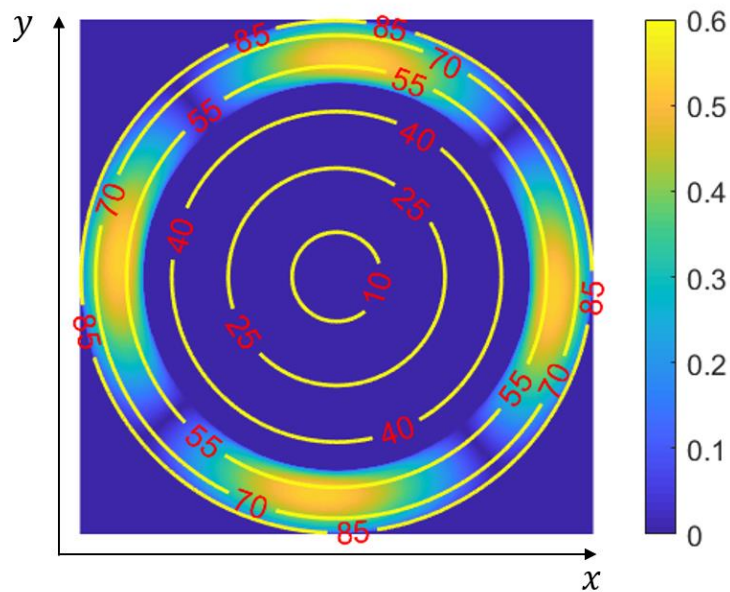


Fig. 6.2. Conversion efficiency as a function of incident angle. The incident light is vertically polarized.

6.2 Average DoCP across a bubble

The conversion efficiency, η , is a function of both θ and ϕ ,

$$\eta = \eta(\theta, \phi) = |\sin \delta(\theta)| |\sin 2\phi|. \quad (6.2.1)$$

where δ is the retardance induced by TIR. For each combination of θ and ϕ , a figure like Fig. 6.2 can be plotted. Meanwhile, for academic purpose, it is interesting to study certain average values of this function.

The average conversion efficiency of all incident angles for a certain LP source is

$$\langle \eta \rangle_{\theta} = \int_{\theta_c}^{\frac{\pi}{2}} |\sin \delta(\theta)| \cdot |\sin 2\phi| \cdot \cos \theta \cdot d\theta, \quad (6.2.2)$$

where θ_c is the critical angle of the air-water interface and $\cos \theta$ is the correction factor for the projection of area. $\langle \eta \rangle_{\theta}$ is numerically evaluated as $0.0668 \cdot |\sin 2\phi|$.

The average conversion efficiency of all possible LP sources for a certain incident angle is

$$\langle \eta \rangle_{\phi} = \frac{1}{2\pi} \int_0^{2\pi} |\sin \delta(\theta)| \cdot |\sin 2\phi| \cdot d\phi = \frac{2}{\pi} |\sin \delta(\theta)|. \quad (6.2.3)$$

The maximum $\langle \eta \rangle_{\phi}$ is 0.34 at $\theta \approx 60^\circ$.

Finally, considering all possible LP sources and all incident angles, the average conversion efficiency is

$$\langle \eta \rangle_{\theta, \phi} = \frac{2}{\pi} \int_{\theta_c}^{\frac{\pi}{2}} |\sin \delta(\theta)| \cdot \cos \theta \cdot d\theta. \quad (6.2.4)$$

$\langle \eta \rangle_{\theta, \phi}$ is numerically evaluated as 0.0425.

Chapter 7. Closing remarks

This dissertation gives a method of separating the specular reflection component on a reflector based on polarimetric imaging and studies the total internal reflection in two underwater scenes. The first topic seems more “engineering-like” while the second one more academic, which may leave some readers thinking why the two seemingly unrelated things could compose a dissertation. There are mainly two reasons. First, both topics are about polarization effects that are happening around us but are overlooked most of the time. We do not need specially-designed experiments to study them; instead, what we need are a piece of glass window for the first study and a fish tank for the second one. On the other hand, glass windows in our daily life are not designed for polarimetric imaging purpose, nor are the waters, and yet extra information can be extracted from the polarization optics “side effects”. Thus, in a sense, the two studies are both about discovering the “uncommons” in the commons. Secondly, the Umov effect in the underwater TIR phenomena is potentially useful to detect a dark object that travels near the water surface. Since the DoCP is inversely proportional to the albedo, the less significant the object is in the irradiance image, the more it stands out in the DoCP image. Still, there could be other usages of the findings in the study of TIR, and hopefully in the future it could be engineered for our benefit.

References

1. E. Collett, "Field guide to polarization," (SPIE, Bellingham, 2005).
2. R. A. Chipman, "Mueller Matrices," in *Handbook of Optics*, M. Bass, ed. (McGraw-Hill Education, New York, 2010).
3. A. Hyvärinen and E. Oja, "Independent component analysis: algorithms and applications," *Neural Networks* **13**, 411-430 (2000).
4. E. C. Cherry, "Some experiments on the recognition of speech, with one and with two ears," *J. Acoust. Soc. Am.* **25**, 975-979 (1953).
5. S. Haykin and Z. Chen, "The cocktail party problem," *Neural Computation* **17**, 1875-1902 (2005).
6. A. J. Simpson, G. Roma, and M. D. Plumbley, "Deep karaoke: Extracting vocals from musical mixtures using a convolutional deep neural network," in *International Conference on Latent Variable Analysis and Signal Separation*, (Springer, 2015), pp. 429-436.
7. D. Maino, A. Farusi, C. Baccigalupi, F. Perrotta, A. J. Bandy, L. Bedini, C. Burigana, G. De Zotti, K. M. Górski, and E. Salerno, "All-sky astrophysical component separation with Fast Independent Component Analysis (FASTICA)," *Mon. Not. R. Astron. Soc.* **334**, 53-68 (2002).
8. S. Makeig, A. J. Bell, T.-P. Jung, and T. J. Sejnowski, "Independent component analysis of electroencephalographic data," *Adv. Neural Info. Proc. Sys.* **8**, 145-151 (1996).
9. Y. Y. Schechner, "Inversion by P4: polarization-picture post-processing," *Phil. Trans. R. Soc. Lond. B* **366**, 638-648 (2011).
10. H. Farid and E. H. Adelson, "Separating reflections from images by use of independent component analysis," *J. Opt. Soc. Am. A* **16**, 2136-2145 (1999).

11. A. Levin and Y. Weiss, "User assisted separation of reflections from a single image using a sparsity prior," *IEEE Trans. Patt. Anal. Mach. Intell.* **29**, 1647 (2007).
12. Y. Shih, D. Krishnan, F. Durand, and W. T. Freeman, "Reflection removal using ghosting cues," in *IEEE Conference on Computer Vision and Pattern Recognition*, (IEEE, 2015), pp. 3193-3201.
13. M. Zibulevsky and B. A. Pearlmutter, "Blind source separation by sparse decomposition in a signal dictionary," *Neural Computation* **13**, 863-882 (2001).
14. Y. Y. Schechner, J. Shamir, and N. Kiryati, "Polarization and statistical analysis of scenes containing a semireflector," *J. Opt. Soc. Am. A* **17**, 276-284 (2000).
15. N. Kong, Y. W. Tai, and J. S. Shin, "A physically-based approach to reflection separation: from physical modeling to constrained optimization," *IEEE Trans. Patt. Anal. Mach. Intell.* **36**, 209-221 (2014).
16. T. Xue, M. Rubinstein, C. Liu, and W. T. Freeman, "A computational approach for obstruction-free photography," *ACM Transactions on Graphics (TOG)* **34**, 79 (2015).
17. A. M. Locke, D. S. Sabatke, E. L. Dereniak, M. R. Descour, J. P. Garcia, T. K. Hamilton, and R. W. McMillan, "Snapshot imaging spectropolarimeter," in *Polarization Analysis and Measurement IV*, (International Society for Optics and Photonics, 2002), 64-73.
18. V. Gruev, R. Perkins, and T. York, "CCD polarization imaging sensor with aluminum nanowire optical filters," *Opt. Express* **18**, 19087-19094 (2010).
19. G. Myhre, W.-L. Hsu, A. Peinado, C. LaCasse, N. Brock, R. A. Chipman, and S. Pau, "Liquid crystal polymer full-stokes division of focal plane polarimeter," *Opt. Express* **20**, 27393-27409 (2012).

20. W. L. Hsu, G. Myhre, K. Balakrishnan, N. Brock, M. Ibn-Elhaj, and S. Pau, "Full-Stokes imaging polarimeter using an array of elliptical polarizer," *Opt. Express* **22**, 3063-3074 (2014).
21. Y. Ding, A. Ashok, and S. Pau, "Real-time robust direct and indirect photon separation with polarization imaging," *Opt. Express* **25**, 29432-29453 (2017).
22. Y. Ding, R. Kerviche, A. Ashok, and S. Pau, "Eavesdropping of display devices by measurement of polarized reflected light," *Applied optics* **57**, 5483-5491 (2018).
23. W. K. Pratt, "Correlation techniques of image registration," *IEEE Trans. Aerosp. Electron. Syst* **10**, 353-358 (1974).
24. A. J. Fitch, A. Kadyrov, W. J. Christmas, and J. Kittler, "Fast robust correlation," *IEEE Transactions on Image Processing* **14**, 1063-1073 (2005).
25. S. R. Curtis and A. V. Oppenheim, "Reconstruction of multidimensional signals from zero crossings," *J. Opt. Soc. Am. A* **4**, 221-231 (1987).
26. J. Canny, "A Computational Approach to Edge Detection," *IEEE Trans. Patt. Anal. Mach. Intell.* **8**, 679-698 (1986).
27. M. Jacob and M. Unser, "Design of steerable filters for feature detection using canny-like criteria," *IEEE Trans. Patt. Anal. Mach. Intell.* **26**, 1007-1019 (2004).
28. P. Bao, L. Zhang, and X. Wu, "Canny edge detection enhancement by scale multiplication," *IEEE Trans. Patt. Anal. Mach. Intell.* **27**, 1485-1490 (2005).
29. W. Rong, Z. Li, W. Zhang, and L. Sun, "An improved CANNY edge detection algorithm," in *IEEE International Conference on Mechatronics and Automation*, (IEEE, 2014), pp. 577-582.
30. W. L. Hsu, K. Balakrishnan, M. Ibn-Elhaj, and S. Pau, "Infrared liquid crystal polymer micropolarizer," *Appl. Opt.* **53**, 5252-5258 (2014).

31. W. L. Hsu, J. Davis, K. Balakrishnan, M. Ibn-Elhaj, S. Kroto, N. Brock, and S. Pau, "Polarization microscope using a near infrared full-Stokes imaging polarimeter," *Opt. Express* **23**, 4357-4368 (2015).
32. E. J. Elton and J. S. Preston, "Effective refractive index and the porosity of coated paper," 4 (*Surfoptic*, 2007).
33. G. Ghosh, "Dispersion-equation coefficients for the refractive index and birefringence of calcite and quartz crystals," *Opt. Comm.* **163**, 95-102 (1999).
34. L. L. Long, M. R. Query, R. J. Bell, and R. W. Alexander, "Optical properties of calcite and gypsum in crystalline and powdered form in the infrared and far-infrared," *Infrared Phys.* **34**, 191-201 (1993).
35. R. Gonzalez, R. Zallen, and H. Berger, "Infrared reflectivity and lattice fundamentals in anatase TiO₂s," *Phys. Rev. B* **55**, 7014 (1997).
36. SCHOTT, "Interactive Abbe-Diagram" (2016), retrieved http://www.us.schott.com/advanced_optics/english/knowledge-center/technical-articles-and-tools/abbe-diagramm.html?us-origin=en-US#.
37. X. D. He, K. E. Torrance, F. X. Sillion, and D. P. Greenberg, "A comprehensive physical model for light reflection," in *SIGGRAPH*, (ACM Press, 1991), pp. 175-186.
38. E. Hecht, *Optics* (Pearson Education, 2016).
39. S.-Y. Lu and R. A. Chipman, "Interpretation of Mueller matrices based on polar decomposition," *J. Opt. Soc. Am. A* **13**, 1106-1113 (1996).
40. Thorlabs, "CMOS Cameras: USB 2.0 and USB 3.0" (2017), retrieved https://www.thorlabs.com/newgrouppage9.cfm?objectgroup_id=4024.

41. M. Sonka, V. Hlavac, and R. Boyle, *Image processing, analysis, and machine vision* (Cengage Learning, 2014).
42. J. G. Nagy and D. P. O'Leary, "Restoring Images Degraded by Spatially Variant Blur," *SIAM Journal on Scientific Computing* **19**, 1063-1082 (1998).
43. M. Levoy and P. Hanrahan, "Light field rendering," in *Proceedings of the 23rd annual conference on Computer graphics and interactive techniques*, (ACM, 1996), pp. 31-42.
44. S. R. Cloude and E. Pottier, "Concept of polarization entropy in optical scattering," *Optical Engineering* **34**, 1599-1611 (1995).
45. J. Bailey, "Astronomical sources of circularly polarized light and the origin of homochirality," *Origins of Life and Evolution of the Biosphere* **31**, 167-183 (2001).
46. J. F. C. Wardle and D. C. Homan, "The nature of jets: Evidence from circular polarization observations," arXiv:astro-ph/0011515 (2000).
47. S. Berthier, M. Thomé, and P. Simonis, "Circular polarization in nature: factual, theoretical and experimental summary," *Materials Today: Proceedings* **1**, 145-154 (2014).
48. D. H. Goldstein, "Polarization properties of Scarabaeidae," *Applied optics* **45**, 7944-7950 (2006).
49. S. A. Jewell, P. Vukusic, and N. Roberts, "Circularly polarized colour reflection from helicoidal structures in the beetle *Plusiotis boucardi*," *New Journal of Physics* **9**, 99 (2007).
50. Y. L. Gagnon, R. M. Templin, M. J. How, and N. J. Marshall, "Circularly polarized light as a communication signal in mantis shrimps," *Current Biology* **25**, 3074-3078 (2015).
51. H. Wynberg, E. Meijer, J. Hummelen, H. Dekkers, P. Schippers, and A. Carlson, "Circular polarization observed in bioluminescence," *Nature* **286**, 641 (1980).

52. W. B. Sparks, J. Hough, T. A. Germer, F. Chen, S. DasSarma, P. DasSarma, F. T. Robb, N. Manset, L. Kolokolova, and N. Reid, "Detection of circular polarization in light scattered from photosynthetic microbes," *Proceedings of the National Academy of Sciences* **106**, 7816-7821 (2009).
53. G. P. Können, *Polarized light in Nature* (CUP Archive, 1985).
54. D. H. Goldstein, *Polarized Light, revised and expanded* (CRC press, 2003).
55. J. A. Lock, "Theory of the observations made of high-order rainbows from a single water droplet," *Applied Optics* **26**, 5291-5298 (1987).
56. A. R. Dahlberg, N. J. Pust, and J. A. Shaw, "Effects of surface reflectance on skylight polarization measurements at the Mauna Loa Observatory," *Optics Express* **19**, 16008-16021 (2011).
57. T. W. Cronin and J. Marshall, "Patterns and properties of polarized light in air and water," *Philosophical Transactions of the Royal Society of London B: Biological Sciences* **366**, 619-626 (2011).
58. G. Horváth and D. Varjú, "Underwater refraction-polarization patterns of skylight perceived by aquatic animals through Snell's window of the flat water surface," *Vision Research* **35**, 1651-1666 (1995).
59. A. G. Cheroske, P. H. Barber, and T. W. Cronin, "Evolutionary variation in the expression of phenotypically plastic color vision in Caribbean mantis shrimps, genus *Neogonodactylus*," *Marine Biology* **150**, 213-220 (2006).
60. B. Hapke, *Theory of reflectance and emittance spectroscopy* (Cambridge University Press, 2012).
61. Y. Ding and S. Pau, "Circularly and elliptically polarized light under water and the Umov effect," *Light: Science & Applications* **8**, 32 (2019).

62. E. Zubko, G. Videen, Y. Shkuratov, K. Muinonen, and T. Yamamoto, "The Umov effect for single irregularly shaped particles with sizes comparable with wavelength," *Icarus* **212**, 403-415 (2011).
63. M. K. Shepard and P. Helfenstein, "A test of the Hapke photometric model," *Journal of Geophysical Research: Planets* **112**(2007).
64. D. Beard and P. Weyl, "Influence of texture on porosity and permeability of unconsolidated sand," *AAPG Bulletin* **57**, 349-369 (1973).